

Chapter 4

Experimental results on TST-2

4.1 Typical pulse

In TST-2, MHD events accompanying magnetic reconnection are often observed. In this chapter, such events are defined as internal reconnection events (IREs). IREs in this study show growths of oscillations on SXR and magnetic signals, followed by a crash of SXR intensity. Figure 4.1 shows a typical discharge with IREs. The events occurred at least twice in this discharge. The plasma current increases slightly in response to a flattening of the current density profile (reduction of the internal inductance). Prior to each IRE, a growth of a mode at a frequency of around 10 kHz was observed on the SXR profile (especially low energy emission measured by the camera without a Be filter) and in magnetic signals. In many cases, the SXR intensities increase, and the mode amplitude grows with a time constant of about 0.4 ms. On the other hand, intensities of magnetic oscillations generally show growths on a shorter time scale (~ 0.1 ms). At the end of the mode growth, energy transport from the central region towards the plasma periphery begins. Following this collapse, the SXR intensities in the outer region increase, and the H_α emission increases. This can be explained by increased interaction of the lost plasma with the vacuum vessel wall. The crash time determined by the duration of the decrease of the SXR intensity near the plasma centre is typically 0.05–0.1 ms.

4.2 Slow time evolution

In order to analyze energy transport on a slow time scale, the profile of $d\langle I_{SX} \rangle / dt$ is plotted in Fig. 4.2, where $d\langle I_{SX} \rangle / dt$ is the time-averaged intensity of SXR obtained by low pass filtering (< 3 kHz). This figure clarifies

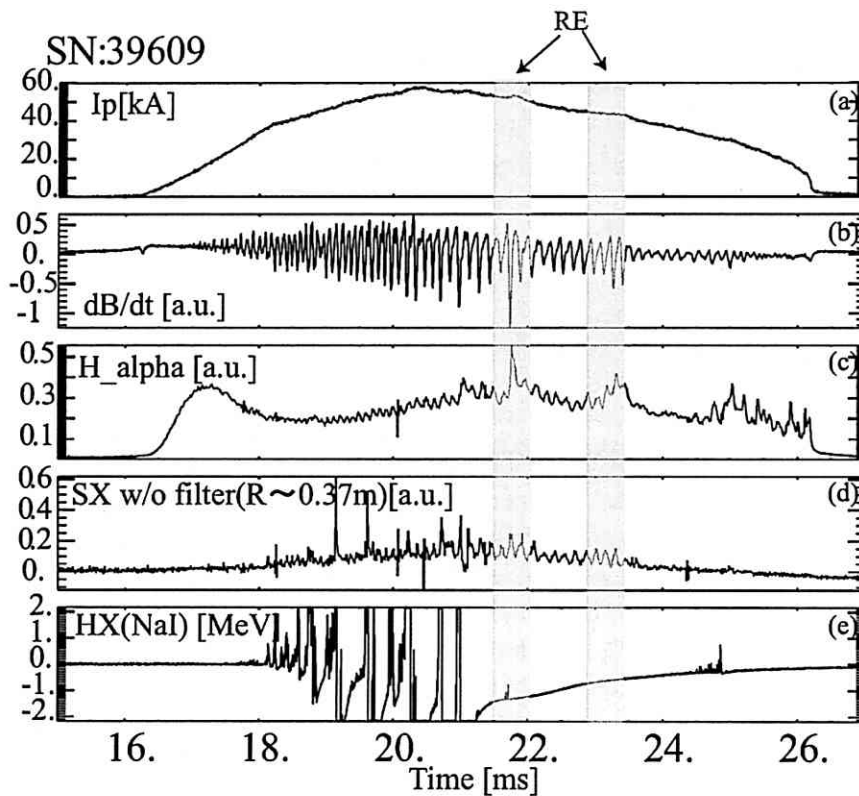


Figure 4.1: Typical discharge waveforms with IREs (SN39609). (a) Plasma current, (b) signal from a magnetic pick-up coil, (c) H_{α} emission, (d) SXR signal from the PIN-diode ($R \sim 0.37$ m), (e) hard X-ray signal from the NaI (Tl) scintillator.

the energy loss process during an IRE. At ~ 22.7 ms (① in Fig. 4.2) the SXR intensity starts to decrease near the centre of the plasma, around Ch.10 ($\rho \sim 0.2$), indicating that a reconnection (small collapse) started around ①. From ② to ③ the region of decreased intensity expands toward the center (major collapse) and then toward the outboard side of the plasma. At ④ the SXR intensity at the plasma centre has recovered.

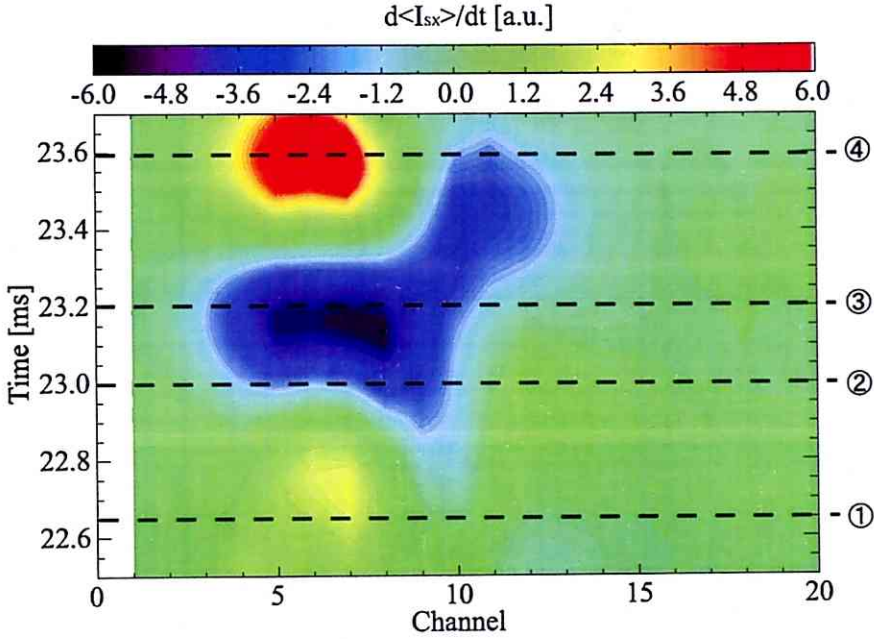


Figure 4.2: Time evolution of the profile of $d\langle I_{SX} \rangle / dt$ during an IRE (SN39609). Channel number represents the radial position (Ch.1 is the innermost tangential sightline).

4.3 Mode analysis

4.3.1 Fourier analysis for precursors

The structure of plasma deformation is characterized by the toroidal mode number n and the poloidal mode number m . The n-coils are very effective to determine the toroidal mode structure. Magnetic fluctuations measured by magnetic probes are generated by a rotation of the deformed plasma. Plasma deformation is caused by instabilities such as the tearing mode. In order to extract the mode number, a power spectrum is obtained by Fourier analysis, as shown in Fig. 4.3. Note that this power spectrum is obtained

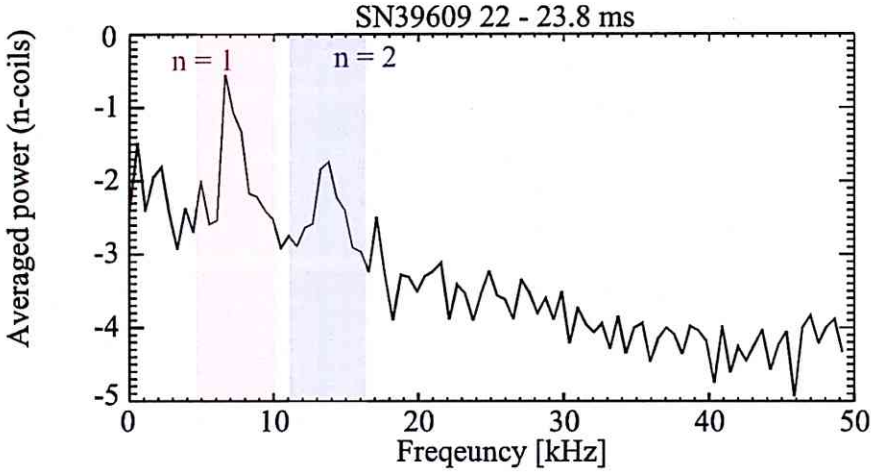


Figure 4.3: Power spectrum of magnetic fluctuation during an IRE. (SN39609)

by averaging the data from seven n-coils (at toroidal angles $\phi = 0^\circ, 30^\circ, 90^\circ, 127.5^\circ, 157.5^\circ, 180^\circ$, and 220°). There are two dominant components (5–10 kHz and 10–17 kHz) in the frequency spectrum. In order to identify the mode number, an ideal sinusoidal wave is assumed and compared with the measured toroidal structure for each dominant frequency component. The fluctuation component \tilde{I} for toroidal mode number n can be expressed as

$$\tilde{I} = I_n \sin(n\phi + \phi_0) \quad (4.1)$$

The two fitting parameters I_n (mode intensity) and ϕ_0 (initial toroidal phase) are determined by best fit to the data. If the mode is growing and rotating in the toroidal direction, an increase of I_n and a periodical change of ϕ_0 should be observed. Figure 4.4 shows the time evolution of the two parameters for

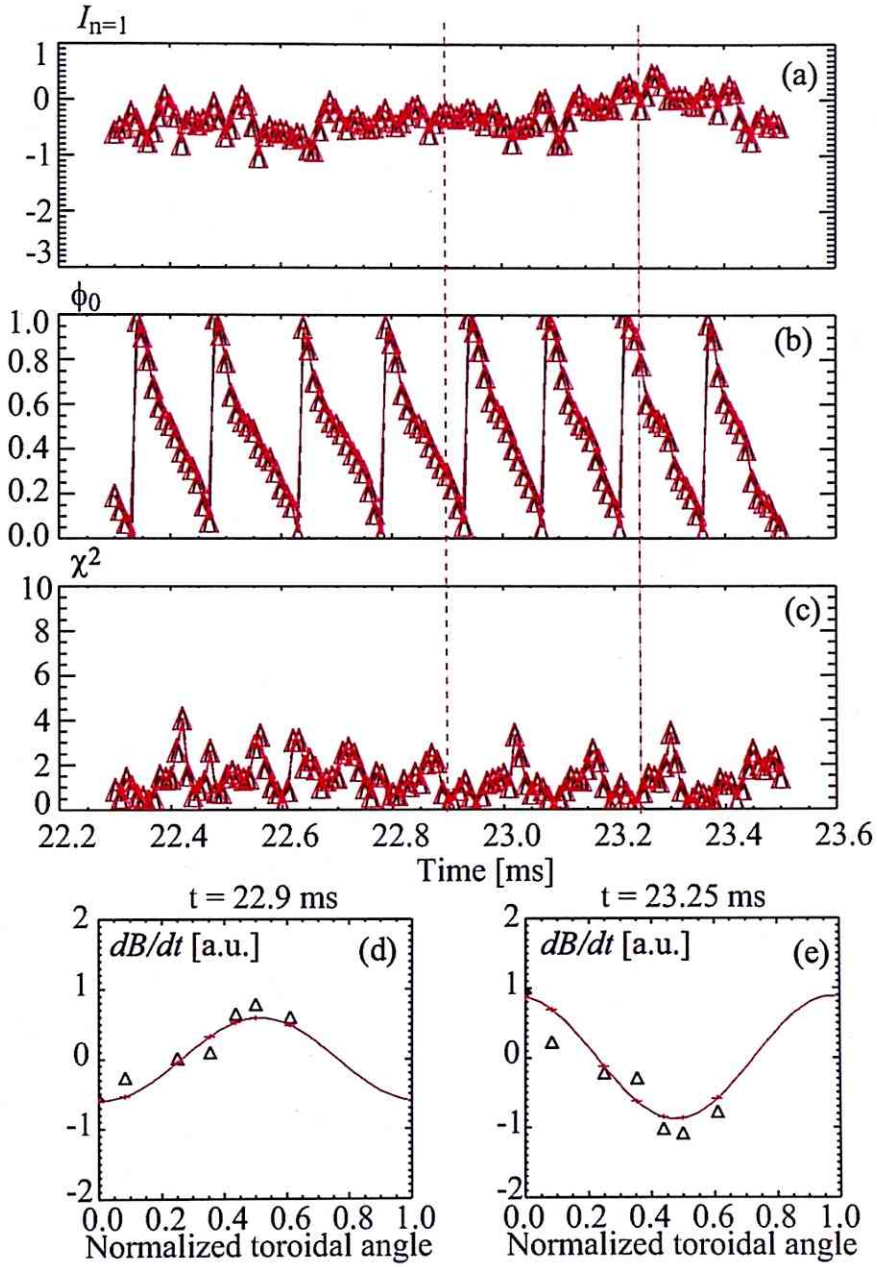


Figure 4.4: Time evolutions of parameters obtained by fitting for $n = 1$: (a) $n = 1$ mode intensity $I_{n=1}$ on logarithmic scale, (b) normalized initial toroidal angle ϕ_0 , (c) fitting error (χ^2), (d), (e) dB/dt [a.u.] along the toroidal direction and fitted lines for $n = 1$ mode at $t = 22.9$ ms and 23.25 ms, respectively. Triangles are experimental signals.

the 5–10 kHz component. If the toroidal mode number were assumed to be $n = 1$, the 5–10 kHz data can be represented well as shown in Fig. 4.4. The mode intensity $I_{n=1}$ shows a growth during $t = 23.1$ – 23.3 ms with a time constant of $\sim 300 \mu\text{s}$, and the initial phase ϕ_0 changes periodically, indicating toroidal rotation of the mode. Toroidal mode profiles from the magnetic fluctuations at $t = 22.9$ ms and 23.25 ms are shown in Fig. 4.4(d) and (e). The 10–17 kHz components correspond to the $n = 2$ mode, as shown in Fig. 4.5. The growth of the $n = 2$ mode starts at $t = 23.1$ ms.

Understanding the mode structure in the plasma is very important, because we can identify which modes are responsible for the collapse. The time evolution of the SXR profile measured by the tangential SXR camera is shown in Fig. 4.6. The internal mode shows a growth from $t \sim 22.5$. From this profile, the $n = 1$ and $n = 2$ components at 5–10 kHz and 10–17 kHz are extracted by Fourier decomposition. If the $n = 1$ and $n = 2$ components overlapped with a constant phase relation, positive components of the two modes strengthen each other, and leads to a large deformation of the magnetic surface. This is the phase alignment predicted by the simulation (see Sec. 2.1.5). The mode profiles during and after the collapse are shown in Fig. 4.7. These mode profiles are taken during the small collapse starting at $t \sim 22.86$ ms. At $t \sim 22.91$ ms, the $n = 1$ and $n = 2$ modes are not well aligned. For example, at $t = 22.97$ ms (red lines in Fig. 4.7), there is a phase reversal near $R_{tan} \sim 430$ mm and cancellation occurs. On the contrary, at $t = 22.91$ ms (green lines) and 23.0 ms (orange lines), there is a phase alignment. Now, the question is when the phase alignment starts. Figure 4.8 shows the time evolution of an SXR channel with strong fluctuations (Ch. 11).

The positive peaks between $n = 1$ and $n = 2$ modes do not show phase alignment until $t \sim 22.6$ ms. However, after this time the positive peaks of the $n = 1$ and 2 modes become aligned with a constant phase difference, as indicated by arrows. This can be seen more clearly by plotting the phase difference between the peaks of $n = 1$ and $n = 2$ modes, as shown by crosses in Fig. 4.9. The phase difference shows a gradual decrease initially, but becomes constant after $t \sim 22.5$ ms ($t = -0.3$ ms). Since the phase alignment occurs before the beginning of the collapse ($t \sim 22.85$ ms), this is the main cause of the collapse. In this discharge, the collapse was small and the oscillations continued after the collapse. In many other discharges with a larger collapse, the phase difference decreases towards zero prior to the collapse. The phase difference is calculated by the SXR signal near the inversion radius. The collapse times have some uncertainty (< 0.1 – 0.15 ms) because the tangential SXR camera measures only one location in the toroidal direction. Since the plasma rotates toroidally, the real collapse time could be earlier than that determined from the SXR profile. It should also be noted that there is a delay

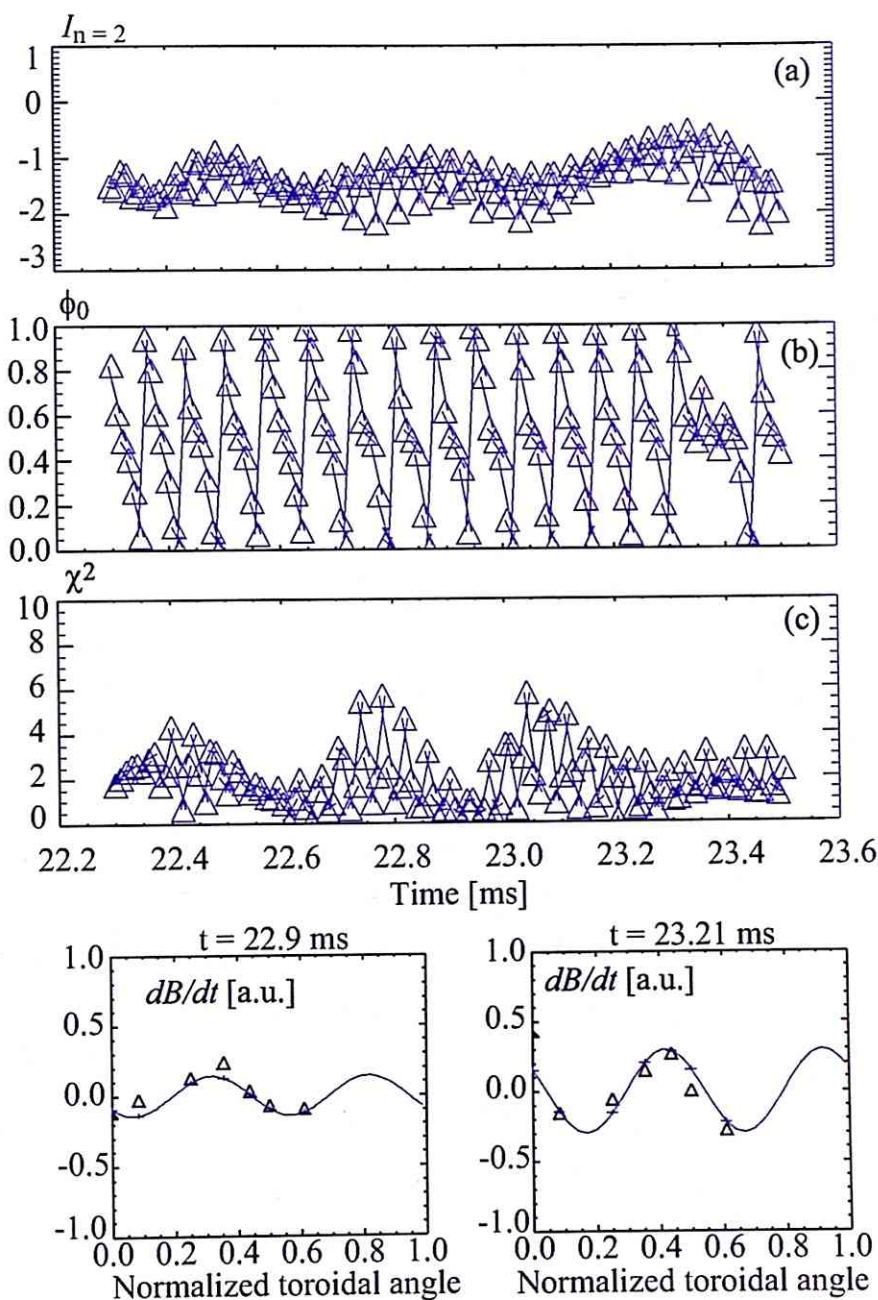


Figure 4.5: Time evolutions of parameters obtained by fitting for $n = 2$: (a) $n = 2$ mode intensity $I_{n=2}$, (b) normalized initial toroidal angle ϕ_0 , (c) fitting error (χ^2), (d), (e) dB/dt [a.u.] along the toroidal direction and fitted lines for $n = 2$ mode at $t = 22.9$ ms and 23.21 ms, respectively. Triangles are experimental signals.

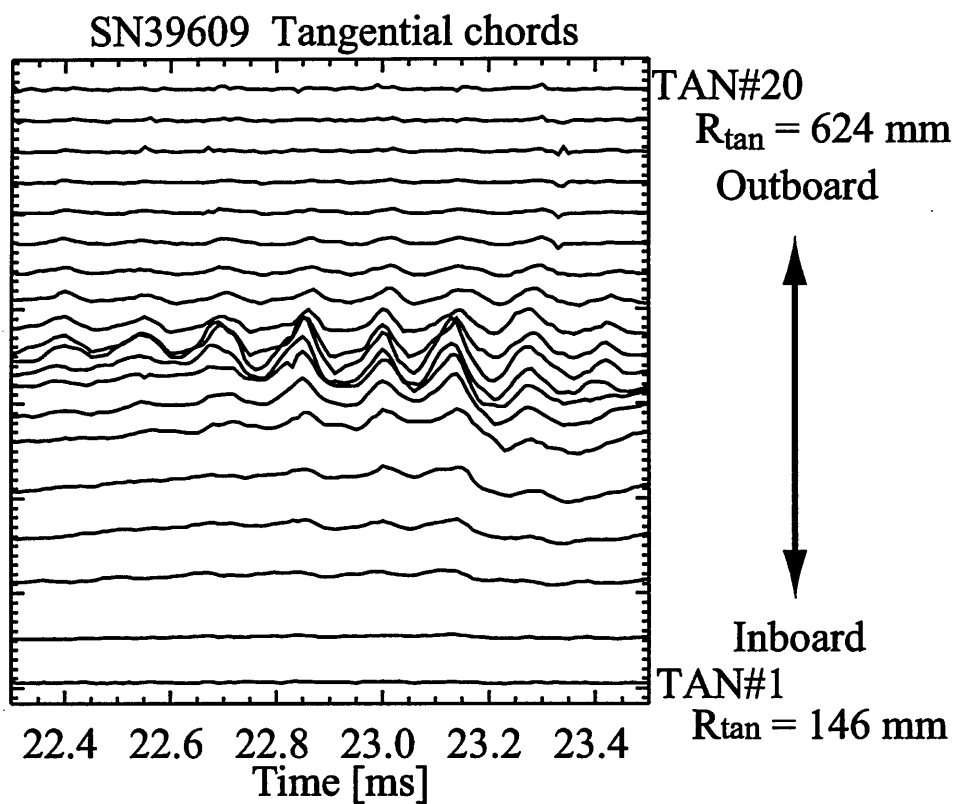


Figure 4.6: Time evolution of SXR profile measured by the tangential SXR camera. (SN39609)

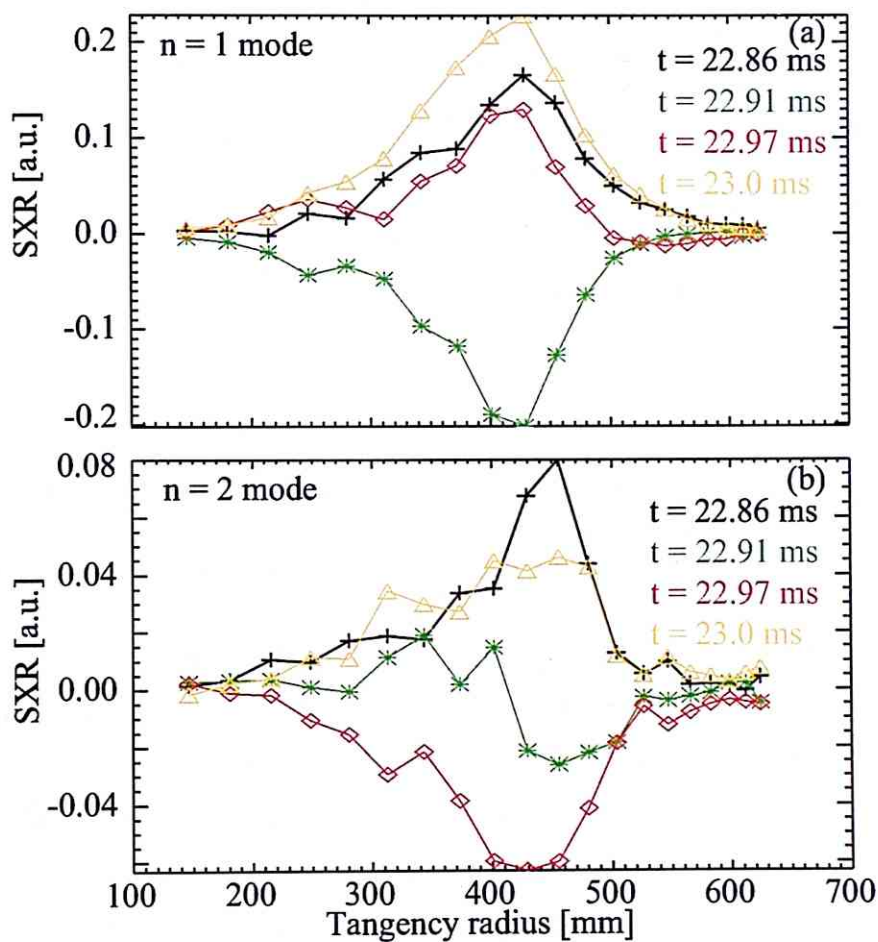


Figure 4.7: (a) $n = 1$ and (b) $n = 2$ mode profiles measured by the tangential SXR camera at $t = 22.86, 22.91, 22.97$ and 23.0 ms.

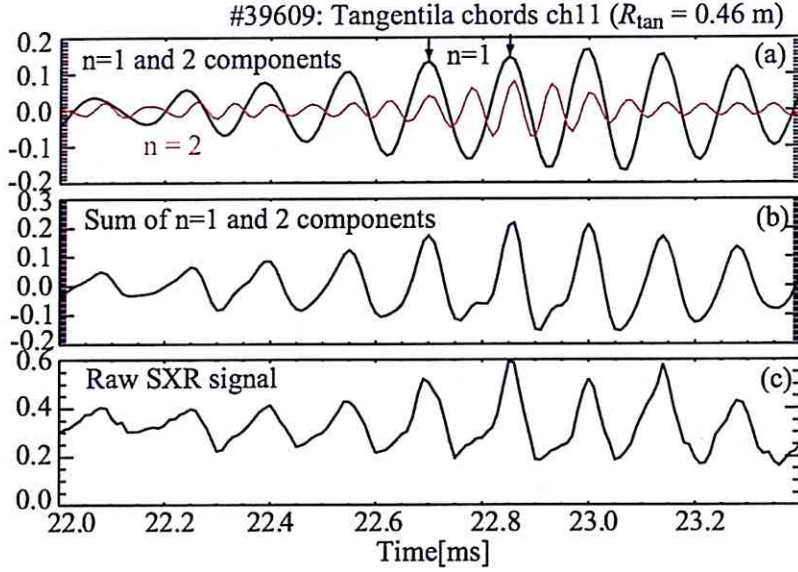


Figure 4.8: Time evolution of $n = 1$ and $n = 2$ modes on SXR. Ch. 11 ($R_{\text{tan}} \sim 0.46$ m). (a) $n = 1$ and $n = 2$ components of SXR signal [a.u.], (b) sum of the two modes, (c) raw SXR signal.

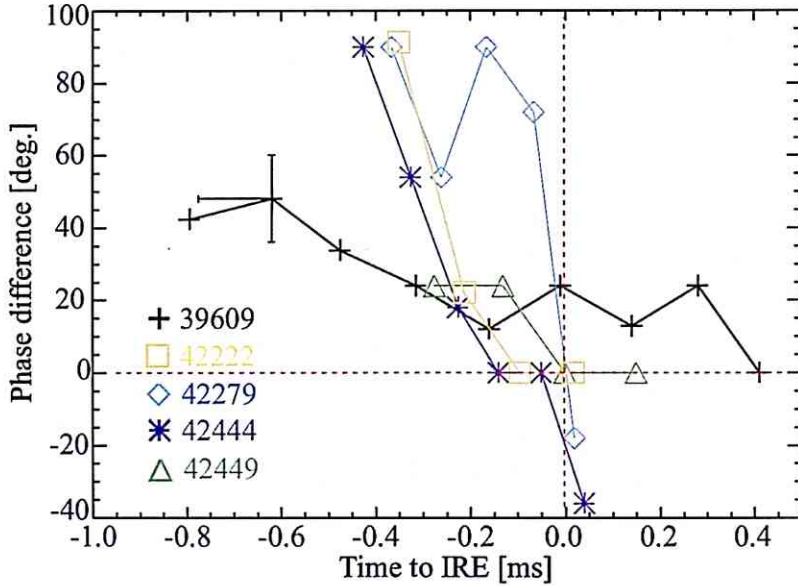


Figure 4.9: Time evolutions of the phase difference between the positive peaks of $n = 1$ and $n = 2$ modes near the inversion radius extracted from SXR data in several discharges.

between the times when the mode intensity shows a local maximum on the time evolutions of SXR and magnetic fluctuation signals. This is presumably because the plasma bulges out on the outboard side due to phase alignment of modes, and the magnetic probe is more sensitive to the outer region of the plasma.

4.3.2 SVD analysis during the growth phase

Magnetic signals reflect the mode behaviour weighted towards the outer region of the plasma, while SXR signals reflect the core behavior. SVD analysis utilizing both SXR and magnetic signals is useful to obtain the correlation between outer and core mode behaviour and to confirm the results of Fourier analysis discussed in the previous section. SVD was executed for the time interval $t = 22.3\text{--}23.2\text{ ms}$. In order to balance the weight between SXR and magnetic signals, magnetic signals are normalized by the maximum amplitude of SXR and magnetic signals, respectively, which shows highest mode intensity during the precursor phase. A high-pass ($> 5\text{ kHz}$) filtering was applied to eliminate the DC component. Chrono and topo for the first four largest singular values are shown in Fig. 4.10. The most dominant mode ($i = 1, \sigma = 11.9$) corresponds to the $n = 1$ mode because the mode structure determined from the topo of n-coils shows one period for one toroidal turn. The topo of SXR profile has a peak intensity at $R_{tan} \sim 0.42\text{ m}$. This result is the same as that obtained by Fourier analysis in the previous section. This mode oscillates in time as shown by the chrono waveform. The second largest mode, $i = 2, \sigma = 8.6$, also corresponds to the $n = 1$ mode as can be seen from the topo of n-coils, but with different phase (90°) from $i = 1$, indicating a toroidal rotation of the $n = 1$ mode. Topo of SXR does not show a similar structure to $i = 1$, and the intensity (amplitude of topo multiplied by the singular value) is weaker by a factor of seven. This indicates the existence of an even mode at $R_{tan} \sim 0.4\text{ m}$. It is appropriate that when the $n = 1$ mode represented by the $i = 1$ structure rotates toroidally by 90° , the SXR profile should look like the topo of $i = 2$. The same analysis can be applied to $i = 3$ and $i = 4$. These modes represent the $n = 2$ mode, as identified by the topo of n-coils. The frequency of oscillation is nearly twice of the $n = 1$ mode, as seen from the chrono.. The $i = 4$ mode shows a clear peak in the SXR profile.

To sum up, the internal mode profiles for the $n = 1$ and $n = 2$ modes were extracted by SVD analysis using both SXR and magnetic data. The mode rotation was revealed by the topo waveforms. Although, Fourier analysis can be used to arrive at the same conclusion, the extraction of coherent modes from internal (SXR) and external (magnetic coils) measurements was also

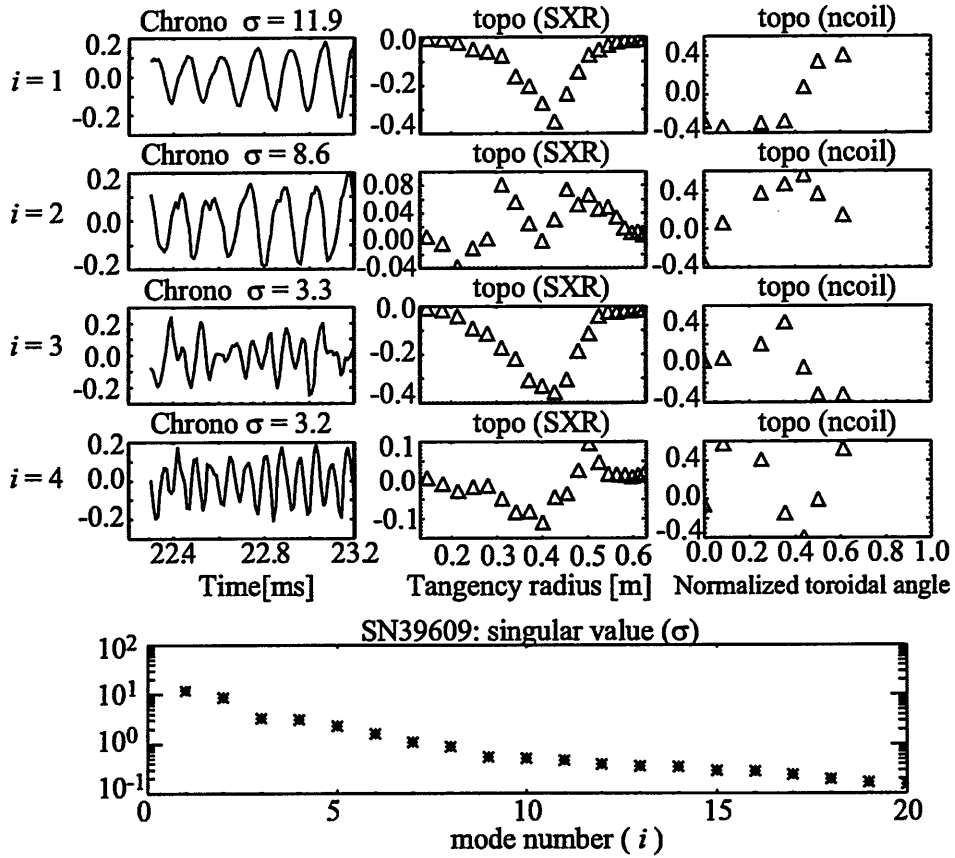


Figure 4.10: Results of SVD analysis for SN39609. Each row corresponds to the mode with i -th largest singular value, and columns represent chrono, topo for the tangential SXR array, and topo for the n-coils. The singular value is shown in the bottom figure.

achieved by the SVD method.

4.4 Correlation between the SXR gradient and ΔI_p

Identification of the condition for occurrence or energy source for IRE is very important for its prevention. The spatial gradient of the SXR profile is defined as dI_{SX}/dr , where I_{SX} is the SXR intensity (without a filter) and R is the tangency radius of the sight line. The gradient is taken from a linear fit to the SXR intensity profile on the outboard side of the torus. An example of the SXR profile and the fitted line is shown in Fig. 4.11.

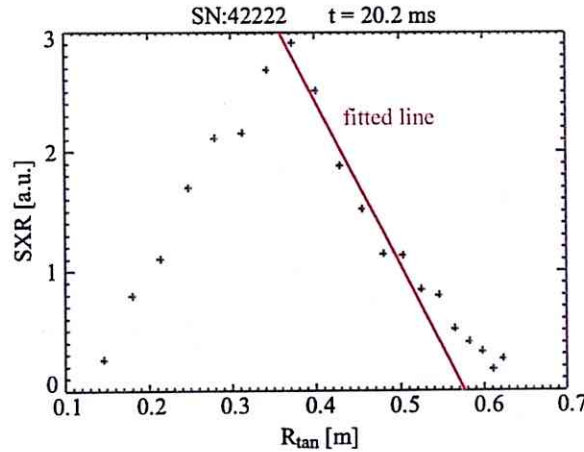


Figure 4.11: SXR profile measured by the tangential camera and a linear fitted line. (SN42222)

Figure 4.12 indicates that a steep profile is necessary to cause an IRE. There is a threshold around $dI_{SX}/dr = 0.02$. This result suggests that the instability is pressure driven, because the SXR intensity depends strongly on the plasma pressure.

Figure 4.13 shows a comparison between dI_{SX}/dr and the increment of plasma current ΔI_p . A positive correlation between dI_{SX}/dr and $\delta I_p/I_p$, which is a measure of the strength of IRE, was confirmed. Here δI_p is the increment of I_p during an IRE. This figure indicates that a steeper SXR profile induces a larger IRE.

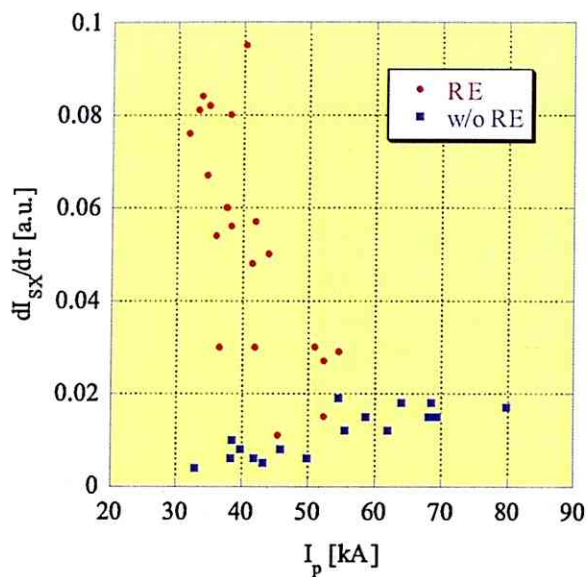


Figure 4.12: dI_{SX}/dr for discharges with RE (red circles) and without RE (blue squares) for various values of I_p .

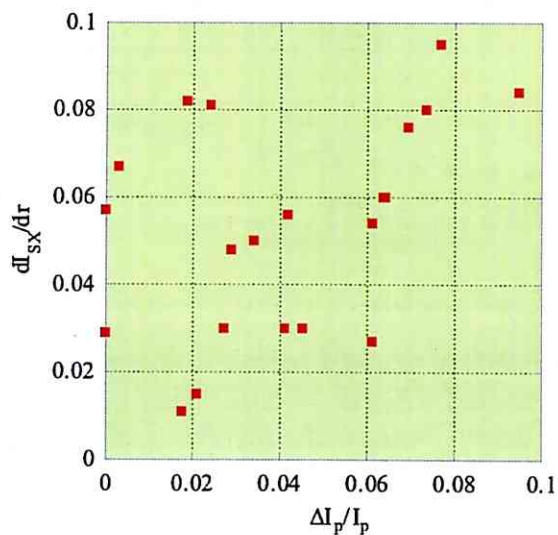


Figure 4.13: Comparison between dI_{SX}/dr and the increment of current ΔI_p for IREs.

4.5 Ion temperature increase

4.5.1 Correlation between T_i and ΔT_i

Magnetic reconnection releases magnetic energy. Increases of the ion-temperature (T_i) have been observed in many experiments as described in Chap. 2. Sudden increases of T_i suggest the occurrence of magnetic reconnection. Figure 4.14 shows the correlation between $\Delta T_i/T_i$ and $\Delta I_p/I_p$, where $\Delta T_i/T_i$ is the relative increment of the ion temperature due to IRE. T_i was measured by the

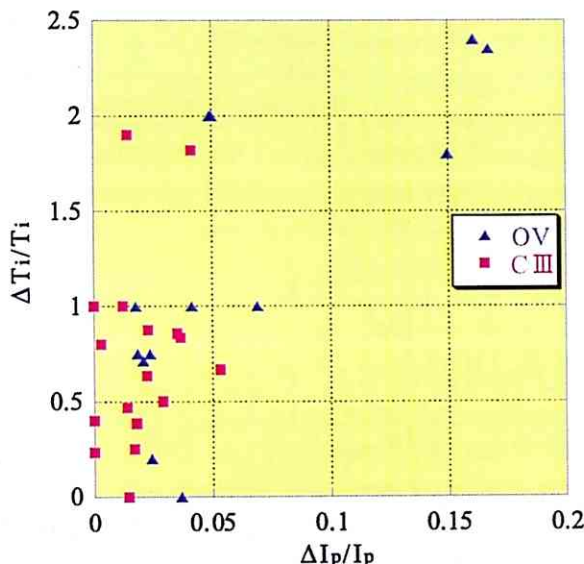


Figure 4.14: Correlation between $\Delta T_i/T_i$ and $\Delta I_p/I_p$

Doppler broadening of CIII and OV lines. Typically T_i (CIII) ~ 20 eV and T_i (OV) ~ 40 – 60 eV before IRE. All data points in the plot show growths of magnetic and/or SXR fluctuations. T_i measured by CIII and OV are correlated positively with $\Delta I_p/I_p$. The highest $\Delta T_i/T_i$ of 2.4 was measured by OV. The scale of IRE, represented by $\Delta I_p/I_p$, is positively correlated with the increase of T_i , indicating that larger IREs result in stronger ion heating.

4.5.2 Time evolution of ion heating compared with detailed SXR profile

Comparison between the detailed SXR profile evolution and the increase of T_i during an IRE is very important for understanding IRE. Moreover, we need to understand what kind of collapse triggers the release of magnetic energy.

Figure 4.15 shows waveforms of a discharge with an IRE. The plasma current

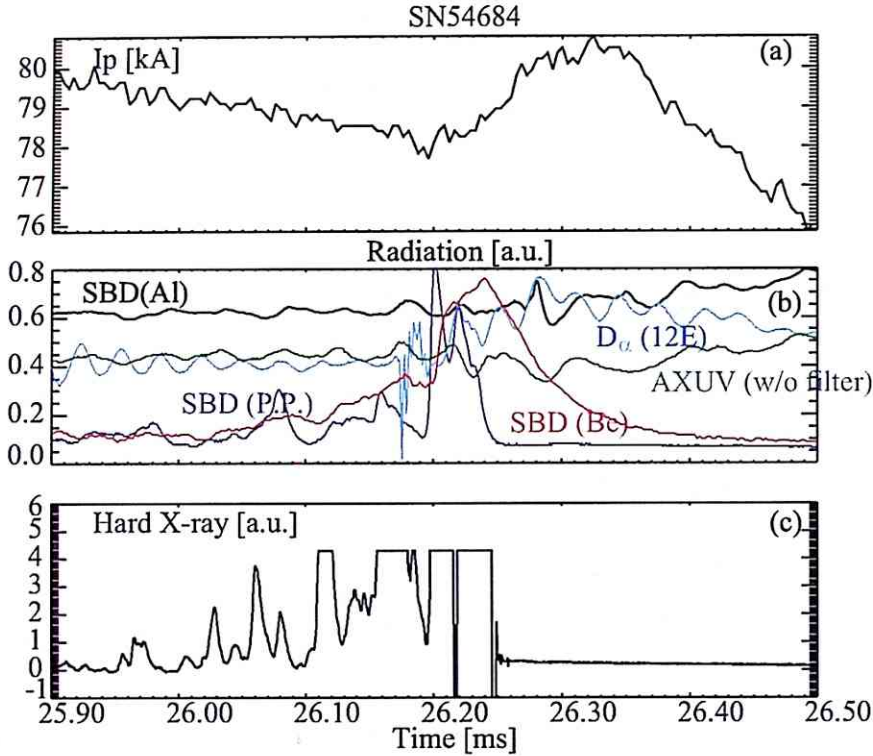


Figure 4.15: Waveforms of a discharge with IRE (SN54684): (a) Plasma current [kA], (b) radiation signals measured by SBD without filter (black), SBD with polypropylene (P.P.) filter (blue), SBD with Be filter (red), AXUV without filter (light blue) and D_{α} , and (c) hard X-ray radiation.

increases by ~ 2 kA from 78 kA at $t \sim 26.2$ ms, indicating a sudden flattening of the current profile as in the previous case. Figure 4.15(b) shows time evolutions of various kinds of radiation. The first notable change is the increase of radiation with high photon energy. SBD with Be and P.P. filters can detect only photons with high energy (greater than 1 keV and 0.1 keV, respectively) as described in Sec. 3.2.3. The intensities start increasing from $t = 26.05$ ms. The increase suggests two possibilities. The first is bremsstrahlung emitted by electrons. These waveforms are similar to hard X-ray radiation detected by the NaI scintillator (Fig. 4.15(c)). When IRE occurs, the plasma is lost along the reconnected magnetic field lines, strike the vacuum vessel wall, and emit high energy photons by thick-target bremsstrahlung. The second possibility is electron acceleration by a process related to magnetic reconnection. The signals detected by AXUV and SBD (Al) without a filter are similar

to the total radiated power, because the energy range of detected photons is broad, from visible light to soft X-rays (< 10 keV). Since there are no significant changes on the time evolution of these signals, we cannot rule out the increased number of high energy photons. In order to check whether the deformed plasma hits the vessel or not, the SXR profile is very useful. Figures 4.16 and 4.17 show time traces of the SXR profile obtained by horizontal and vertical SXR cameras, respectively.

It is clear that a magnetic reconnection with a major collapse starts from $t \sim 26.2$ ms. The green arrows indicate flows of particles and heat caused by magnetic reconnection. The point is whether there are any signs of collapse affecting the outside of the plasma boundary. A deformation due to the modes do not appear near the outside boundary of the plasma during the period $t = 26.05$ – 26.2 ms on either of the measured SXR profiles, suggesting that high energy electrons are generated during this phase. Turning to the correlation between the SXR profile and the ion temperature, T_i was measured from the Doppler broadening of the OV line (278.1 nm) by the spectrometer. The spectra measured at two time slices are shown in Fig. 4.18. T_i was determined from the width of the Gaussian fit to the measured spectrum. T_i increased from 56 ± 12 eV before IRE to 133 ± 18 eV after IRE. The time evolution of T_i is shown in Fig. 4.17, showing an increase of T_i from $t = 26.2$. It should be noted that there must be a delay from the time of reconnection to the beginning of T_i increase, because it takes a finite time (equilibration time) for the directed ion energy to be converted to thermal energy (see Sec. 1.1.5). At $t \sim 26.18$ ms (indicated by the first vertical arrow), there is a small increase of SXR at H#18 ($Z = -0.32$ m). This is the expected reconnection time.

To sum up, a weak increase of SXR with high energy (> 0.1 keV) was observed just before a major collapse, suggesting a change in the electron energy spectrum. A T_i increase starts from the time when a major collapse starts, and there is a time delay (~ 0.02 ms) from the time of occurrence of magnetic reconnection.

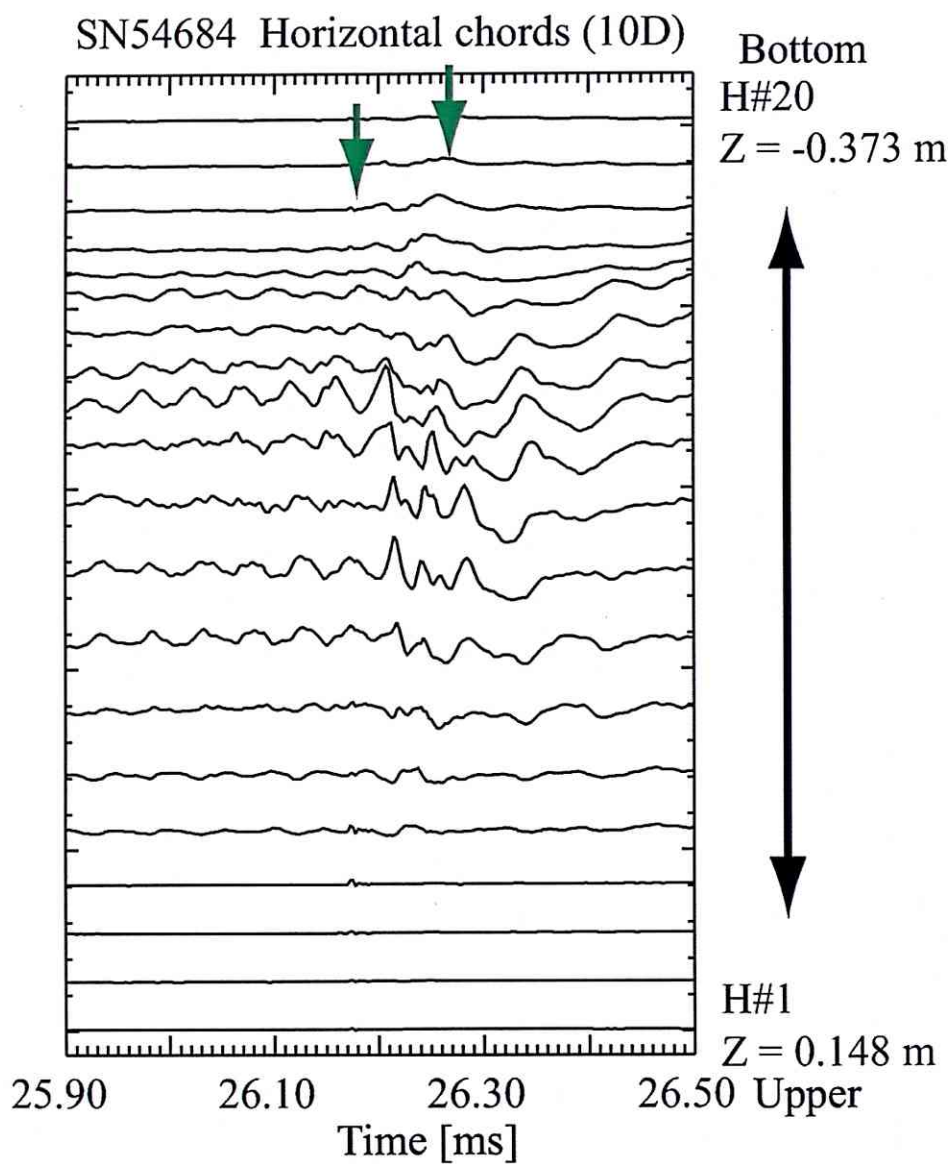


Figure 4.16: Time evolutions of SXR signals measured by the horizontal SXR camera (10D). (SN54684)

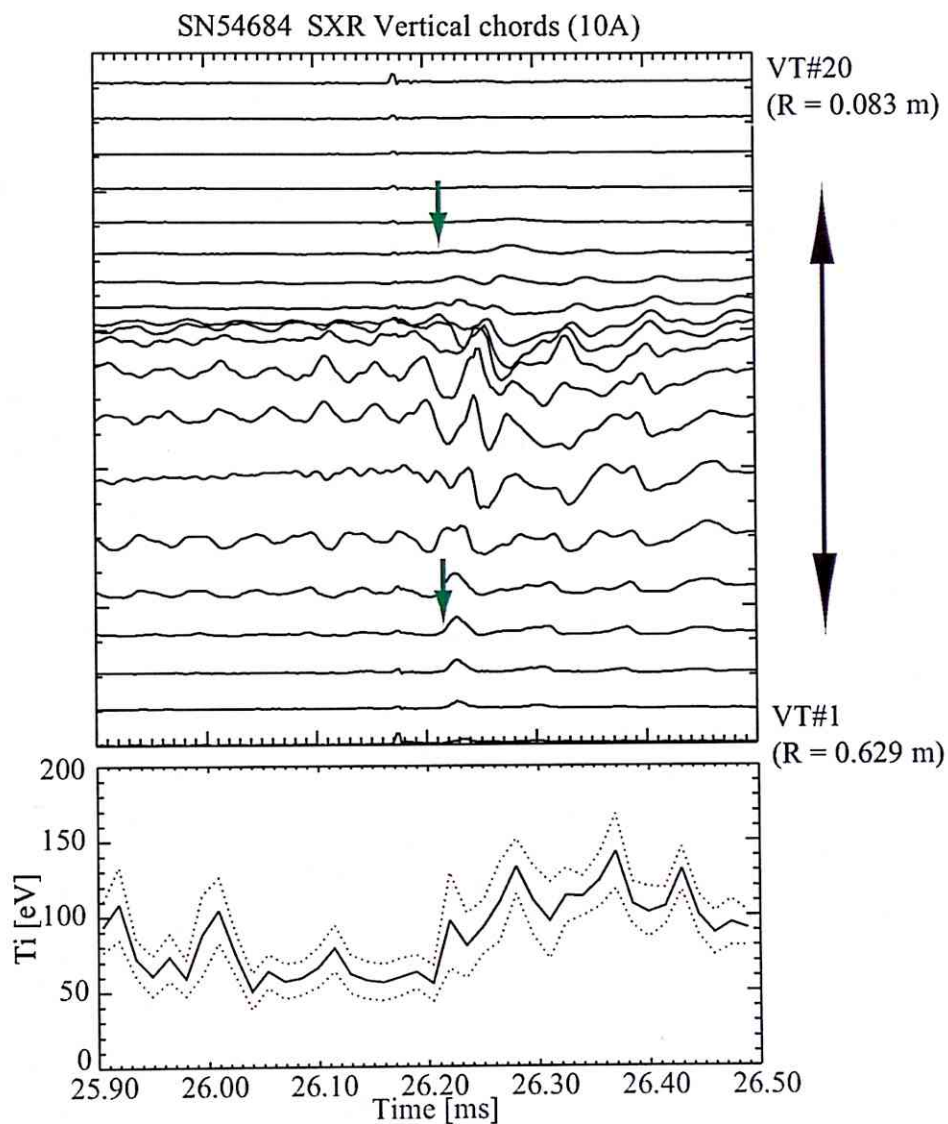


Figure 4.17: Time evolutions of SXR signals measured by the vertical SXR camera (10A) and T_i . (SN54684)

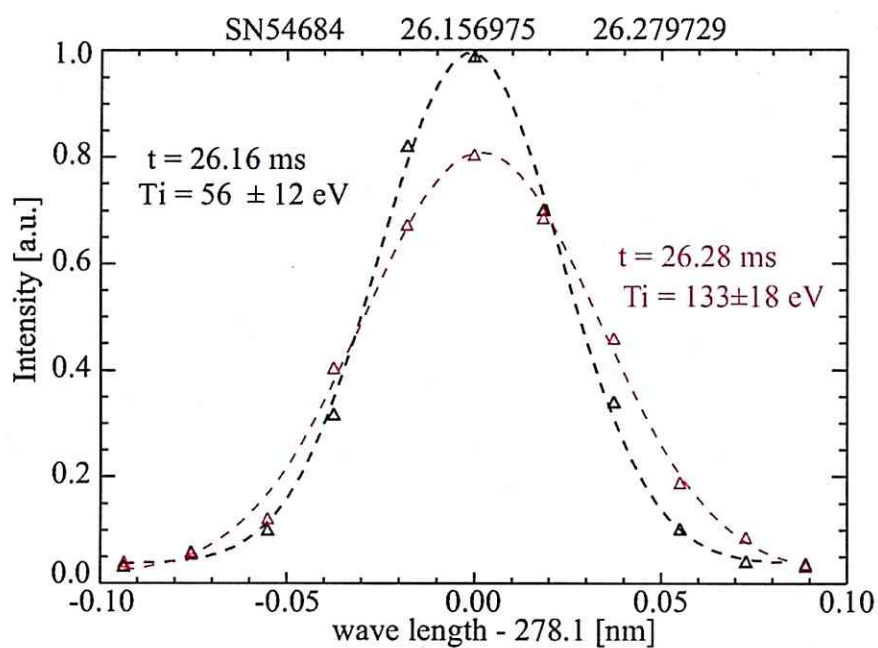


Figure 4.18: Line spectra (OV at 278.1 nm) measured by the spectrometer at $t = 26.16$ and 26.28 ms.

Chapter 5

Experimental setup on MAST

5.1 Plasma performance

MAST (Mega Ampere Spherical tokamak) [83][84][85] at EURATOM/UKAEA Fusion Association, Culham Science Centre, U.K. is being operated to investigate the physics of high temperature, high β plasmas in low-aspect ratio configurations. Typical MAST parameters are summarized in Table. 5.1. Figure 5.1 is a photograph of MAST. Ohmic heating (OH) and neutral beam

parameter	value
Major radius R	~ 0.85 m
Minor radius a	~ 0.65 m
Aspect ratio A	~ 1.3
Toroidal magnetic field B_t	< 0.52 T
Plasma current I_p	~ 0.1 MA
Discharge duration	< 0.7 s
Toroidal β	$< 17\%$

Table 5.1: Typical parameters of MAST.

(NB) injection are used to heat the plasma and drive the plasma current. Two NB injectors are on loan from Oak Ridge National Laboratory [86]. One of them has been used on START, the predecessor to MAST. The ORNL injector typically delivers up to $P_{NB} = 1.5$ MW of deuterium NB power into the plasma, at an accelerator voltage of 40 kV. One of the two beams has been replaced by a JET-style PINI (Positive Ion Neutral Injector) with dramatically improved performance.

On MAST, H-mode (high confinement mode) plasmas with high β and long confinement time are readily obtained. The density profile has flat

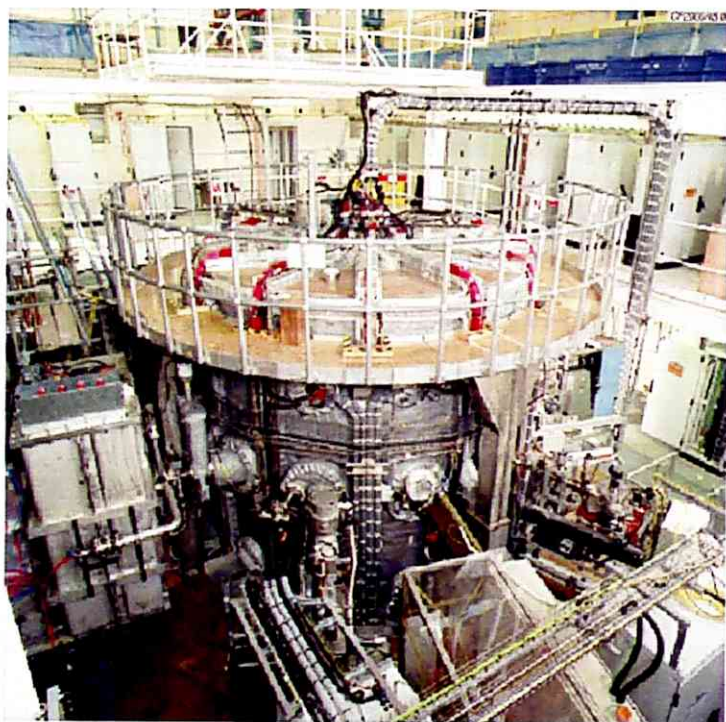


Figure 5.1: Picture of Mega Ampere Spherical Tokamak (MAST)

region in the core and a steep gradient near the edge. In almost all cases the edge localized mode (ELM) is observed as spikes of D_α emission. MAST can operate in the double null (two X-points) configuration to divert flows of particle and energy to the divertor. The poloidal field coils are located inside the vacuum vessel. The vacuum vessel is a large cylindrical tank with a diameter of $\sim 4\text{m}$, so there is very good access for diagnostic systems.

5.2 Diagnostics

5.2.1 Thomson scattering system

On MAST, electron density and temperature profiles are measured by two types of Thomson scattering (TS) systems. The TS system utilizes scattering of a laser beam by electrons. The Ruby TS system has high spatial resolution of $\sim 3\text{mm}$ [87], but can obtain only one time point in a shot for each laser. Figure 5.2 shows the electron pressure profile measured by the Ruby TS system. The Ruby TS system can measure a detailed profile with a

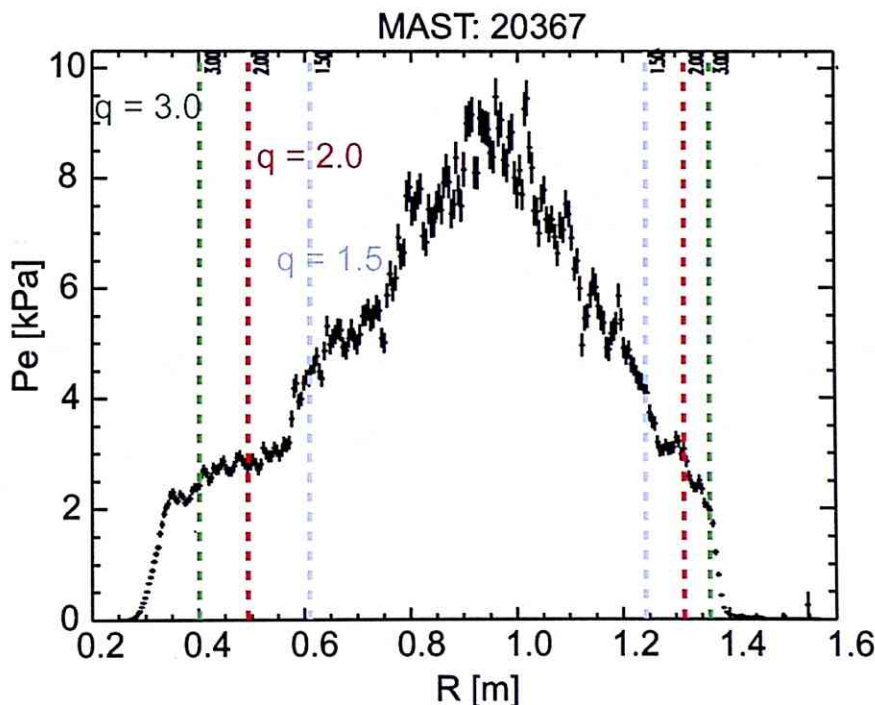


Figure 5.2: Electron pressure profile measured by the Ruby TS system in MAST (#20367).

spatial resolution of a few cm, and is useful for investigating the structure of instabilities. The colored vertical lines indicate positions of selected rational surfaces ($q = 1.5, 2$, and 3). Near the $q = 2$ surface there is flat region indicating the presence of a magnetic island (tearing mode). The other TS system uses a YAG laser with 50 Hz repetition rate [88]. MAST has used four YAG lasers in 2007 (200 Hz repetition rate with four lasers), and eight lasers from 2008. Both TS systems cover the full plasma diameter.

5.2.2 Magnetic coils

Four kinds of Mirnov coils are installed on MAST. All Mirnov coils except for OMAHA coils measure the vertical component of magnetic field (B_z)

Centre column toroidal Mirnov array

Twelve coils are installed on the centre column distributed in the toroidal direction, and measure the time derivative of magnetic field (dB/dt). The coils are not uniformly spaced and are located at toroidal angles $\phi = 10^\circ, 50^\circ, 70^\circ, 110^\circ, 130^\circ, 170^\circ, 190^\circ, 230^\circ, 250^\circ, 290^\circ, 310^\circ$, and 350° . The origin of the toroidal angle is at Sector 1 (North: $\phi = 0^\circ$, West: $\phi = 90^\circ$). The locations of coils are shown in Fig. 5.3. The coil is wound on a ceramic form

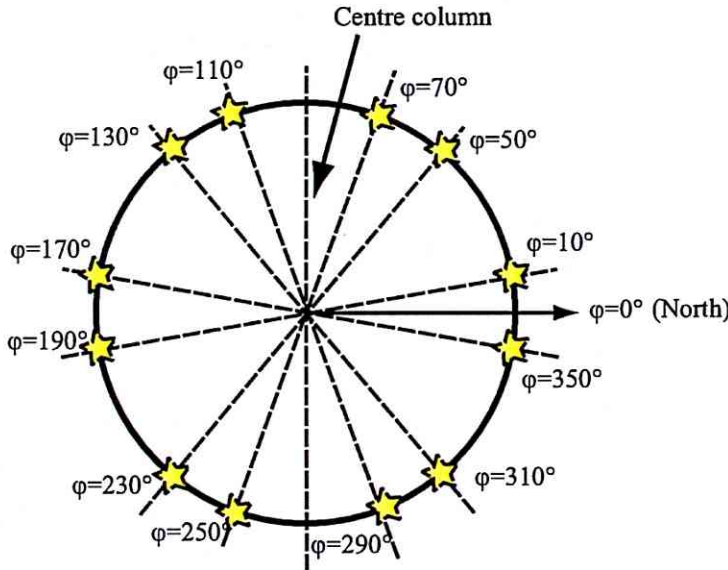


Figure 5.3: Locations of coils in the toroidal Mirnov array on the centre column.

(Fig. 5.4). The diameter of the wire is ~ 0.35 m. The coil has two layers

of 35 turns each, giving $NA \sim 0.14 \text{ m}^2$ and 71 T/s/V . N is the number of turns and A is the cross sectional area of the ceramic form, respectively. The

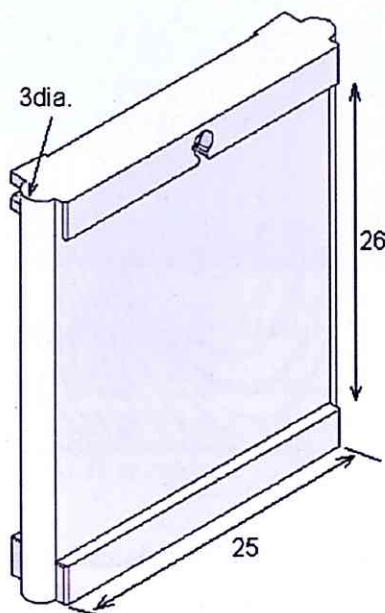


Figure 5.4: Ceramic form for coils of the toroidal Mirnov array.

toroidal mode number can be determined by measuring the phase shift along the toroidal direction.

Outboard toroidal Mirnov array

In order to acquire information on mode structure on the outboard side, Mirnov coils on the outboard side at toroidal angles $\phi = 150^\circ$, 270° , and 330° are used.

Vertical Mirnov array

To understand the poloidal mode structure, MAST is equipped with 58 Mirnov coils distributed in the poloidal direction at Sector 9 ($\phi = 270^\circ$). The locations of coils in the vertical Mirnov array are shown in Fig 5.5. However, it is not easy to determine the poloidal mode number m because the cross section of the plasma is not circular, and the difference of magnetic fields on the inboard side and the outboard side is significant. It is essential to develop a method for determining m .

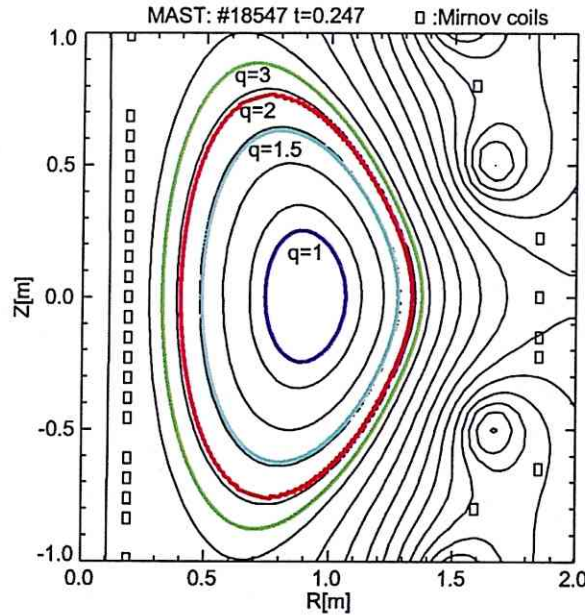


Figure 5.5: Locations of coils in the vertical Mirnov array (plotted as squares) on the centre column..

OMAHA coils

OMAHA (Outboard Mirnov Array for High-frequency Acquisition) coils are used to measure high frequency modes such as the energetic particle mode (EPM), the toroidal Alfvén eigenmode (TAE), and the compressional Alfvén eigenmode (CAE) [90]. OMAHA coils used until 2007 were located at $\phi = 243.5^\circ, 247.5^\circ, 267.5^\circ, 277.7^\circ, 292.5^\circ, 306^\circ, 324^\circ, 336^\circ, 357^\circ$, and 6° . All coils except one are located above the mid-plane at $Z = 200$ mm ($R \sim 1.7$ m). The toroidal spacing between adjacent coils was $\delta\phi = 18^\circ$, and these coils enabled determination of toroidal mode numbers of up to $n = 10$. In 2008, these coils were moved to $\phi = 54.5^\circ, 122.5^\circ, 127.5^\circ, 142.5^\circ, 147.5^\circ$, and 172.5° . Two coils, one above and another below the mid-plane ($Z = \pm 200$ mm) are installed at each toroidal angle. Figure 5.6 shows the head of an OMAHA coil. It contains three orthogonal coils to measure the toroidal, vertical, and radial components of the magnetic field. The centre of each coil is at the same (R, Z, θ) . The coil is connected to a triaxial cable for impedance matching. NA of the coils are $6.5 \times 10^{-3} \text{ m}^2$, $7.5 \times 10^{-3} \text{ m}^2$, and $8.8 \times 10^{-3} \text{ m}^2$, respectively. We should note the frequency dependence of gain (NA).

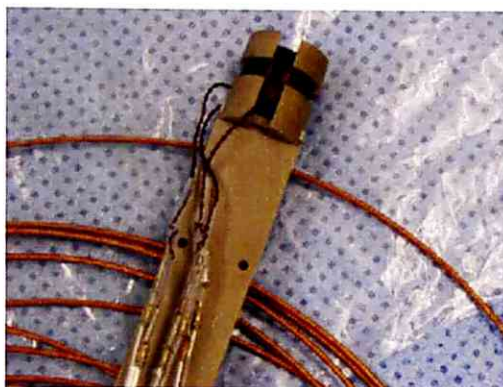


Figure 5.6: Photograph of the head of an OHAMA coil.

5.2.3 SXR cameras

MAST has three kinds of SXR cameras.

Horizontal SXR camera

The horizontal SXR camera measure the SXR profile along the vertical direction at Sector 12. The camera has two diode detectors (Centronics L35-5T, 18 channels) and a common slit ($1\text{ mm} \times 3\text{ mm}$). Figure 5.7 shows the sightlines of the detectors. In practice 32 (16×2) channels are used. From the top side of the poloidal section, channels are numbered HCAMU#16 to HCAMU#1, and HCAML#1 to HCAMU#16. In order to reject low energy photons, $15\text{ }\mu\text{m}$ thick beryllium (Be) filters are installed in front of the detectors. The transmittance of the Be filter is shown in Fig. 5.8. For MAST parameters (usually, $T_e > 1\text{ keV}$), such a thickness is need to limit the output signal from the detectors. Photons with $\sim 1\text{ keV}$ can pass the filter. The frequency response determined by the amplifier is up to $\sim 100\text{ kHz}$.

Vertical SXR camera

The vertical camera located at the same poloidal cross section as the horizontal camera measures the radial profile. There are two cameras (inner and outer) at the same port. The inner camera has 12 channels and the outer camera has 8 channels. The filter is the same as the horizontal camera ($15\text{ }\mu\text{m}$ Be) and the slit ($1\text{ mm} \times 3\text{ mm}$) is located 62.0 mm away from the diode. The detector is the same as the horizontal camera (Centronics L35-5T) but with less channels. The outer camera views the plasma on the low field side edge from the top of the machine. Only the inner vertical SXR camera sightlines

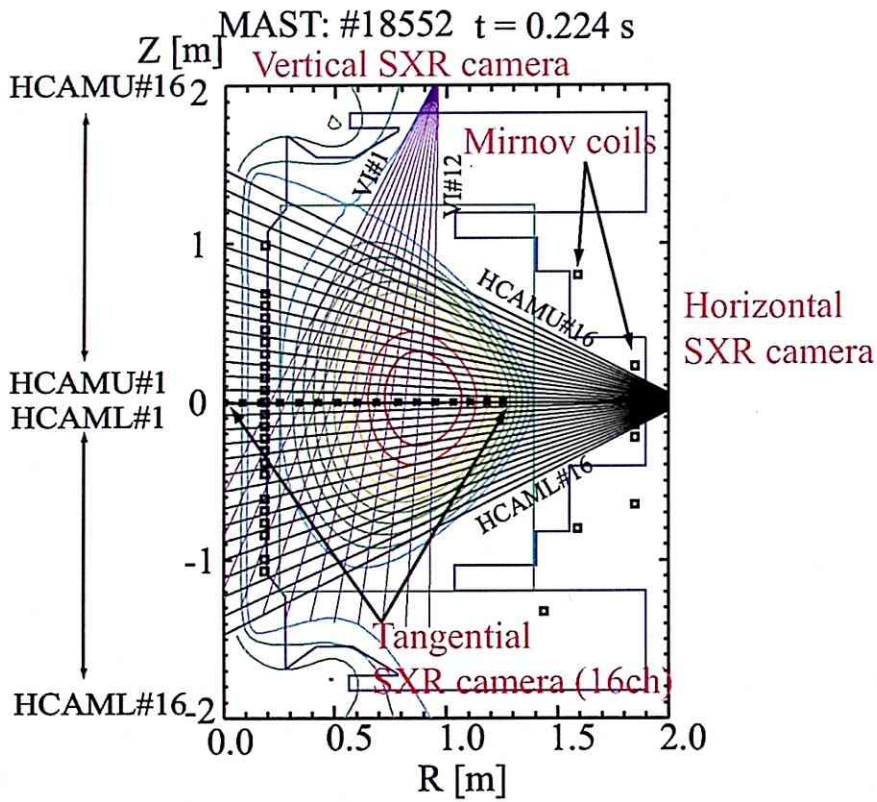


Figure 5.7: Sightlines of the horizontal, vertical (only inner arra), and tangential SXR cameras.

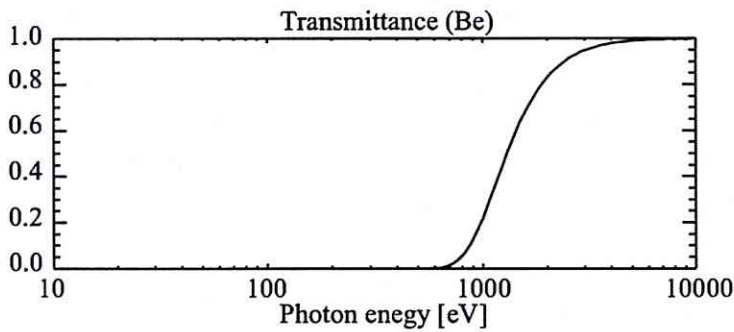


Figure 5.8: Transmittance of $15\mu\text{m}$ thick Be foil as a function of photon energy.

are shown in Fig. 5.7.

Tangential SXR camera

The radial profile of SXR is also measured by a tangential camera with sightlines in the toroidal direction. The positions (tangency points) of the sightlines are shown in Fig. 5.7. Note that the measured region is different from the horizontal and vertical cameras. The radial profiles of modes are obtained using this camera. However it is not possible to measure the SXR from near the edge of the plasma with this camera.

5.2.4 Magnetic reconstruction by EFIT

Plasma parameters can be inferred from the measured magnetic fields by solving for MHD equilibrium, as described in Sec. 1.2.3. The Grad-Shafranov equation is solved subject to boundary conditions specified by magnetic measurements. EFIT (equilibrium fitting code) [91] is a standard code used in many tokamak experiments, including MAST. There are at least three types of EFIT. Normal EFIT uses measured magnetic fields as constraint. Kinetic EFIT (kEFIT) uses not only magnetic measurements but also kinetic measurements such as the pressure profile measured by Thomson scattering. A detailed description of kEFIT can be found in [92]. The third one is EFIT constrained by the measured q profile, and is under development. From the fall of 2008, q profile measurements by the Motional Stark Effect (MSE) system [93][94] is becoming available in MAST. The MSE system measures the spatial profile of polarization angle of a single component of the Stark spectrum, from which the plasma current density profile can be derived. DIII-D tokamak already employs the MSE constrained EFIT [95]. In this thesis, normal EFIT and kEFIT are used for mode and profile analyses.

5.2.5 Comparison between SXR and TS measurements

While the TS system measures the radial profile of electron temperature and density, the horizontal SXR camera with up to 32 channels does measures the vertical profile of SXR. Generally instability analysis requires profile information. For example the tearing mode creates a magnetic island and a flattened region in the pressure profile. The SXR profile is very useful for determining the mode position. Therefore, it is important to compare the measured radial pressure profile and the mode profile from SXR. In this study we use the normalized poloidal flux (ψ) as a reference for comparison. We assume that each SXR channel reflects the behavior at the minimum poloidal

flux position along the sight line. The poloidal flux profile is obtained from EFIT. Once we determine the relationship between the SXR channel and ψ , we can determine the radial position with the same ψ . We can describe the radial position of each SXR channel by this method.

5.3 Error field correction coils

In tokamaks, symmetry of the magnetic field is very important for plasma stability. In reality, however, there are small error fields induced by minor coil positioning errors and the surrounding environment. In order to eliminate the error fields, MAST employs error field correction coils (EFCC) which can induce radial magnetic fields. A photograph of EFCC is shown in Fig. 5.9. The yellow coils outside the vacuum are EFCCs at $R = 2.93$ m. There are



Figure 5.9: Photograph of the error field correction coil on MAST

four coils (two pairs) and the currents can be adjusted. With the current on one pair of coils (3 turns), an $n = 1$ perturbation can be induced. It is possible to increase the current to $I_{max} = 15 \text{ kA} \cdot \text{turns}$. The geometry is shown in Fig. 5.10. In normal plasma discharges, we generate $1 \text{ kA} \cdot \text{turns}$ and $3.5 \text{ kA} \cdot \text{turns}$ for each pair of coil for error field correction.

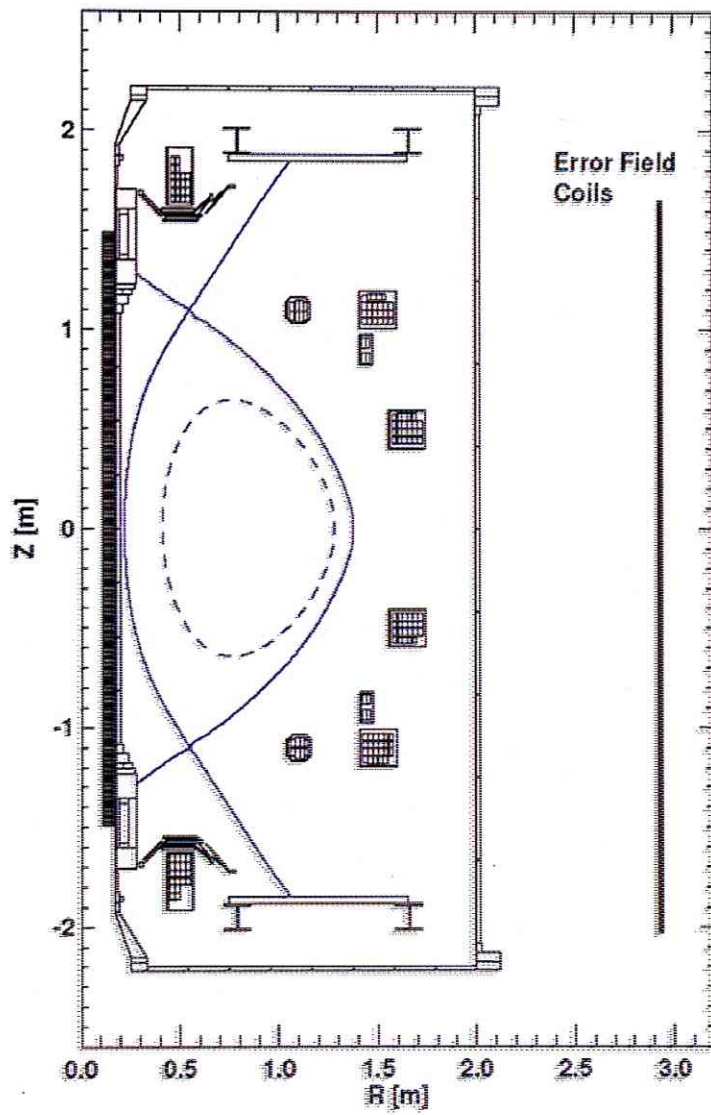


Figure 5.10: Location of EFCC on a poloidal cross section.

Chapter 6

Poloidal mode analysis based on magnetic probe data

6.1 Introduction

In tokamak plasmas with non-circular plasma cross section, it is not simple to determine the poloidal mode number (m), which is very important for analysis of MHD instability. For example, a resistive MHD instability known as the neo-classical tearing mode (NTM) limit achievable β in tokamak plasmas. In a previous study [97], the mode structure localized at a rational surface was expressed by a Green's function. It includes the three dimensional (toroidal) effect due to the helical magnetic field in conventional tokamak experiments with high aspect ratio. In STs, the magnetic field configuration is different from the conventional tokamak because of the highly asymmetric magnetic field line pitch angle. In order to deal with such a configuration, a new method was developed to evaluate the poloidal mode number and its amplitude. Reference [98] used axisymmetric filamentary currents on a resonant surface calculated by EFIT to generate magnetic fluctuations. The poloidal positions of these filaments are determined by tracing magnetic field lines on this surface. The number of alternating positive and negative filament pairs coincides with the mode number. However, there are two defects. Firstly, it does not represent continuous distribution of the filamentary currents. Continuous profiles of the plasma, such as temperature, pressure, and density, must be taken into consideration. Secondly, three dimensional effects are ignored. Since the tearing instability perturbation is helical, the magnetic field measured by Mirnov coils have contributions from other toroidal angles. This effect is very large in the low aspect ratio ST configuration, and must be taken into account. The goal of this work is to determine the poloidal

mode number from the measured Mirnov coil signals.

6.2 Magnetic field line tracing in MAST

It is necessary to determine the trajectories of filamentary currents on the rational surface in order to represent the mode structure. Tearing modes are localized near rational surfaces such as $q = 1, 1.5, 2, 3$, where q is the safety factor. We calculate trajectories of magnetic field lines on each rational surface in MAST plasma from the vertical (B_z), radial (B_r) and toroidal (B_t) components of the magnetic field by

$$\frac{d\phi}{d\theta} = \frac{r}{R} \cdot \frac{B_t}{-B_r \sin \theta + B_z \cos \theta} \quad (6.1)$$

where ϕ , θ , r , and R are the poloidal angle, toroidal angle, distance from the magnetic axis to a point on the rational surface under consideration, and the distance from the symmetry axis of the torus to the point. Figure 6.1 shows the trajectories of the magnetic field lines on several rational surfaces given by an EFIT reconstruction. The origin of the poloidal turn (poloidal angle normalized by 2π) corresponds to $z = 0$ on the outboard side of the torus. The derivative with respect to the poloidal turn is much larger on the inboard side than the outboard side. This is a characteristic for the ST configuration.

6.3 Axisymmetric and helical configurations with distributed filamentary currents

The mode structure can be represented by filamentary currents as

$$I_{mnl}(\theta, \phi) = I_0 \exp i[m\theta - n(\phi + \phi_l + \phi_0)] \quad (6.2)$$

where I_0 , ϕ_l , ϕ_0 are the maximum filamentary current, equally-spaced toroidal angles up to the number of filaments (if the number of filaments is four, $\phi_l = 0, \pi/2, \pi, 3\pi/2$), and the toroidal offset angle as the initial condition, respectively. However, this formula is not accurate for a low aspect ratio, non-circular cross section plasma. In general toroidal plasmas we can represent ϕ as a function of θ as shown in Fig. 6.1. Therefore, we can describe the distribution of helical filamentary currents as

$$I_{mnl}(\theta, \phi) = I_0 \exp in[\phi(\theta) - \phi + \phi_l + \phi_0]. \quad (6.3)$$

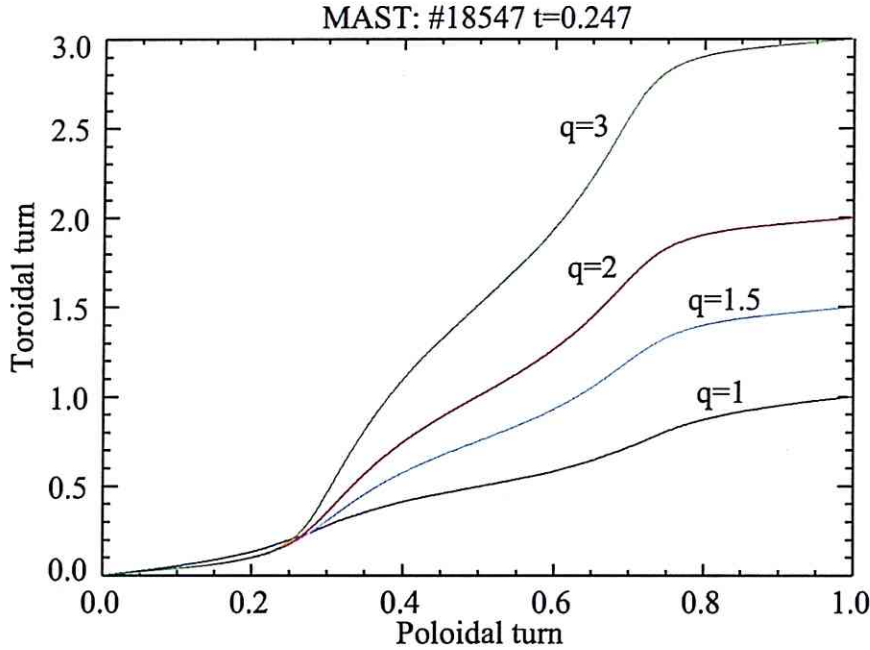


Figure 6.1: Trajectories of magnetic field lines on several rational surfaces based on EFIT reconstruction (#18547 at $t = 0.247$ s). The trajectory on the $q = 1$ surface (blue) is added artificially.

This formula indicates that the distribution of filamentary currents in a poloidal cross section is described by the trajectories shown in Fig. 6.1. Once the initial toroidal position (ϕ_0) is selected, the poloidal angles of other filaments are determined by distributing them in toroidal intervals. The interval depends on m and the number of distributed filaments. We compare two ways of representing a filamentary structure. One is by axisymmetric filaments parallel to the toroidal direction, which is almost the same as that used in [98]. The other is by helical filaments parallel to the magnetic field lines. Since magnetic islands induced by tearing modes have helical structures, trajectories of filamentary currents should have the same structure. Figure 6.2 shows a comparison of axisymmetric and helical distributed filamentary currents with a $3/2$ mode at the $q=1.5$ surface. Generally, density of the filaments is lower on the outboard side. The bottom figures show the distributions of filamentary currents in a poloidal cross section (left) and as a function of poloidal angle (right).

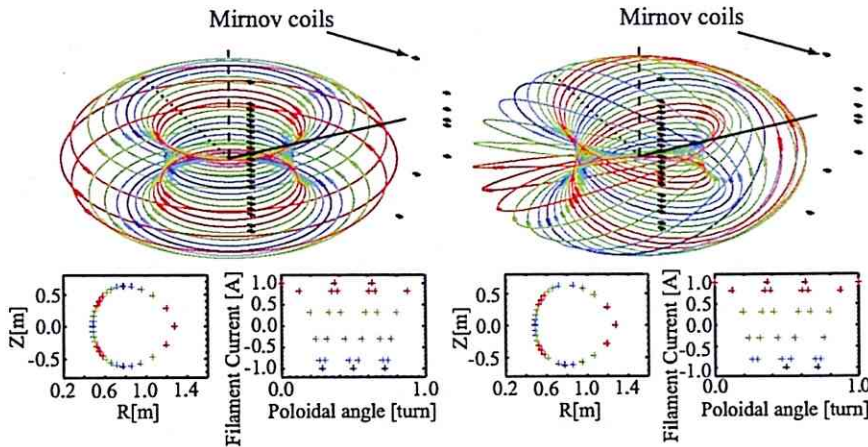


Figure 6.2: Models with axisymmetric (left) and helical (right) filaments. Bottom figures are filamentary currents on a poloidal cross section (left) and as a function of the poloidal angle.

6.4 Comparison between axisymmetric and helical filamentary current models

It is more realistic to use filamentary currents along the helical magnetic field lines to represent magnetic field fluctuations observed by Mirnov coils. On the other hand, helical filaments require heavier computation. Thus, it is important to evaluate the helical effect qualitatively. We calculated magnetic fields at equal poloidal intervals (72 points) at r_m (minor radius) = $0.8m$ using a representative MAST configuration as an example (Fig.6.3). Figure 6.4 shows the poloidal (B_p) and toroidal (B_t) components of the magnetic field calculated for the $m/n = 3/2$ mode as functions of the poloidal angle. Fifteen filaments were used. The major difference between these calculations is the existence of finite B_t for the helical filament model, which is absent for the axisymmetric filament model. It is generated by the vertical component of the current. Crosses denote poloidal angles corresponding to filaments with the maximum or minimum currents. The dotted lines indicate the amplitude of the adjusted axisymmetric model such that the discrepancy with the helical model is minimized in a least-squares sense. Even when the amplitude is adjusted, the discrepancy between these two models is significant especially on the high-field side because of the unique three dimensional effects of the helical configuration. Filaments close by with alternating currents can easily offset the fields at the measurement points.

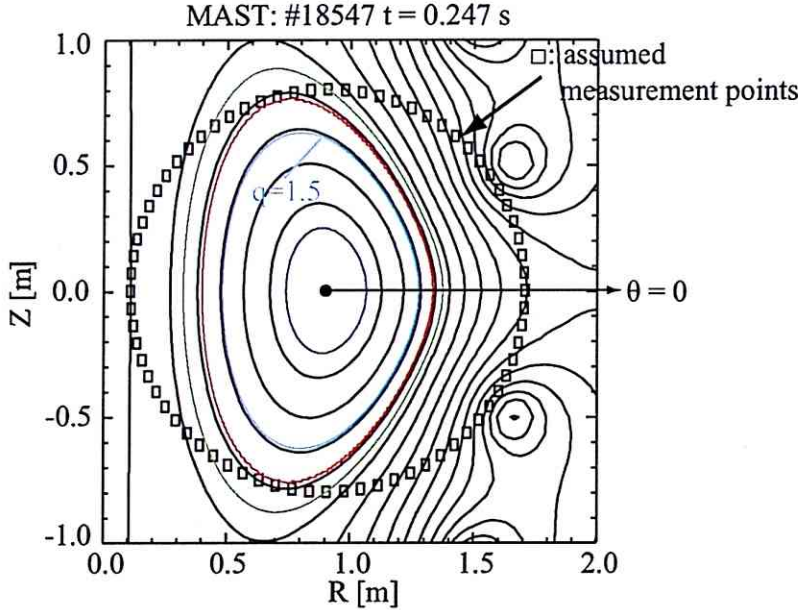


Figure 6.3: Positions of the $q = 1.5$ rational surface (light blue) and points used for magnetic field calculation (squares).

6.5 Fitting by axisymmetric and helical models assuming one mode

We performed fitting calculations for the MHD mode observed by Mirnov coils as magnetic fluctuations with a frequency of a few kHz before an MHD event ($t \sim 0.25$ s in Fig. 6.5), which leads to a collapse. The mode intensity and the mode number were determined from the maximum current among the distributed filaments and the toroidal offset angle ϕ_0 . The toroidal offset angle determines the filament positions uniquely, and the time evolution describes toroidal rotation of the mode. The results are shown in Fig. 6.5. Before applying this method, we used a band-passed filter (1-5 kHz) and performed time integration to obtain the filtered magnetic field. In most cases, good agreement between the measured and calculated data was obtained by assuming only the $m/n=2/1$ mode. In order to evaluate the goodness of fit, the residual error χ^2 with the following definition was calculated.

$$\chi^2 = \sum_i \frac{[y_{fit}(i) - y_{raw}(i)]^2}{\sigma^2} \quad (6.4)$$

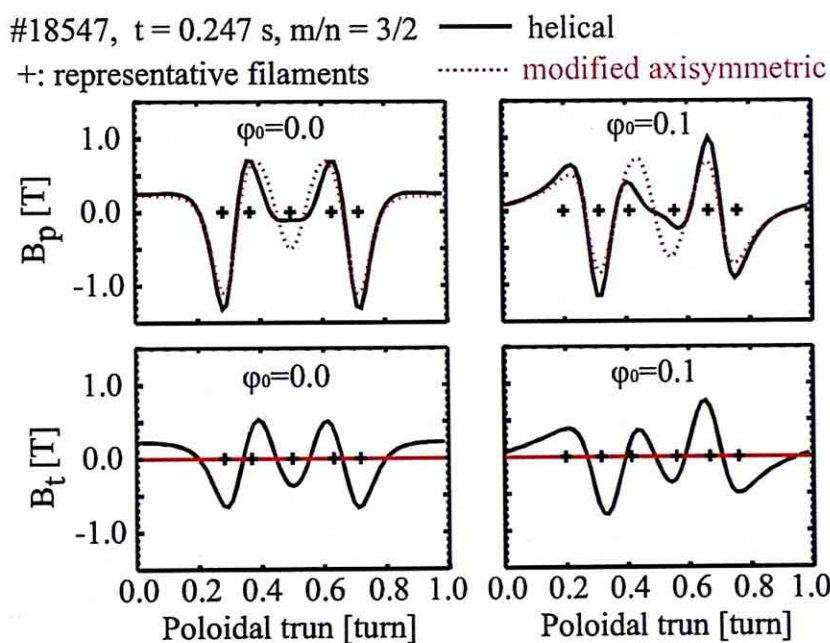


Figure 6.4: Poloidal (upper) and toroidal (lower) components of the magnetic field calculated for helical and axisymmetric filamentary current models at $r_m = 0.8$ m using 72 poloidal points.

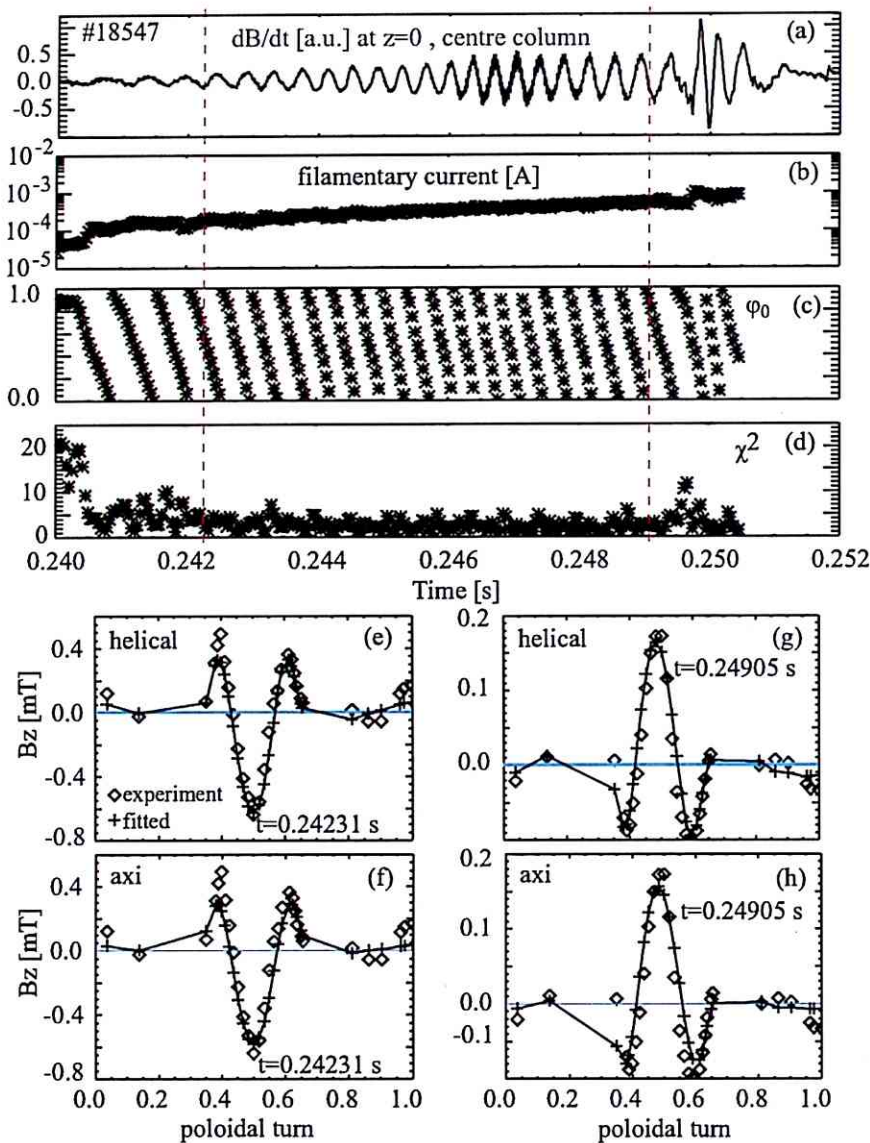


Figure 6.5: Time evolution of the fitted result using helical filaments assuming the $m/n = 2/1$ mode. (a) Mirnov coil signal at $z = 0$, dB/dt [a.u.], (b) the maximum current of filamentary currents [A], (c) the toroidal offset angle [turns], and (d) χ^2 (fitting error). Bottom figures show the vertical component of the magnetic field (B_z) measured by Mirnov coils compared with fitted results using helical and axisymmetric filaments at $t = 0.24231$ s (e, f) and 0.24905 s (g, h), indicated by red dashed lines in the top figures.

$$\sigma^2 = \sum_i \frac{y_{raw}(i)^2}{N} \quad (6.5)$$

The rms fluctuation amplitude was used for the variance. In the present analysis, the phase relations and the amplitudes of these calculated and measured results look acceptable when χ^2 is less than 10. The mode intensity [Fig. 6.5(b)] shows a linear growth with a time constant of about 2 ms. The monotonic increase of the toroidal offset angle (ϕ_0) in Fig. 6.5(c) represents toroidal rotation of filamentary currents. The accuracy of the fit is acceptable from $t = 0.2405$ to 0.2505 s as shown in Fig. 6.5(d). A comparison of fits with helical and axisymmetric models indicates superiority of the helical model. For instance, at $t = 0.24231$ s, χ^2 is 1.91 for helical and 3.78 for axisymmetric models, and at $t = 0.249050$ s, χ^2 is 2.16 for helical and 5.84 for axisymmetric models. In some cases, the residual error for the axisymmetric model becomes very large. Therefore, helical filaments are used hereafter.

Low χ^2 and reasonable fitting results have been obtained for not only the 2/1 mode but also for other modes such as $m/n = 3/2$. This is one of the most important modes for limiting the performance in MAST discharges. Figure 6.6 indicates the presence of two kinds of modes, with a low frequency mode (~ 1 kHz) and a high frequency mode (~ 20 kHz) frequency, and shows the time evolution of the fitting results. The high frequency component with 18–25 kHz was used for fitting. The toroidal offset angle indicates toroidal rotation of the mode. Note that the range of normalized toroidal angle is 0 – 0.5 because there are two toroidal periods for $n = 2$. The two flattened areas in the electron pressure profile measured by Thomson scattering (Fig. ??) suggest the existence of magnetic islands. The position of the $q = 3/2$ rational surface from EFIT reconstruction is close to the flattened area. As shown in Fig. 6.6, χ^2 is greater than 10. The reasons for such a poor fit for the 3/2 mode compared to the 2/1 mode are: (1) EFIT has a large uncertainty in determining the positions of rational surfaces in a region of low magnetic shear because it uses magnetic fields measured outside the plasma. (2) The signal on Mirnov coils for the 3/2 mode is smaller than that for the 2/1 mode because the 3/2 mode is located farther inside the plasma (farther away from the Mirnov coils).

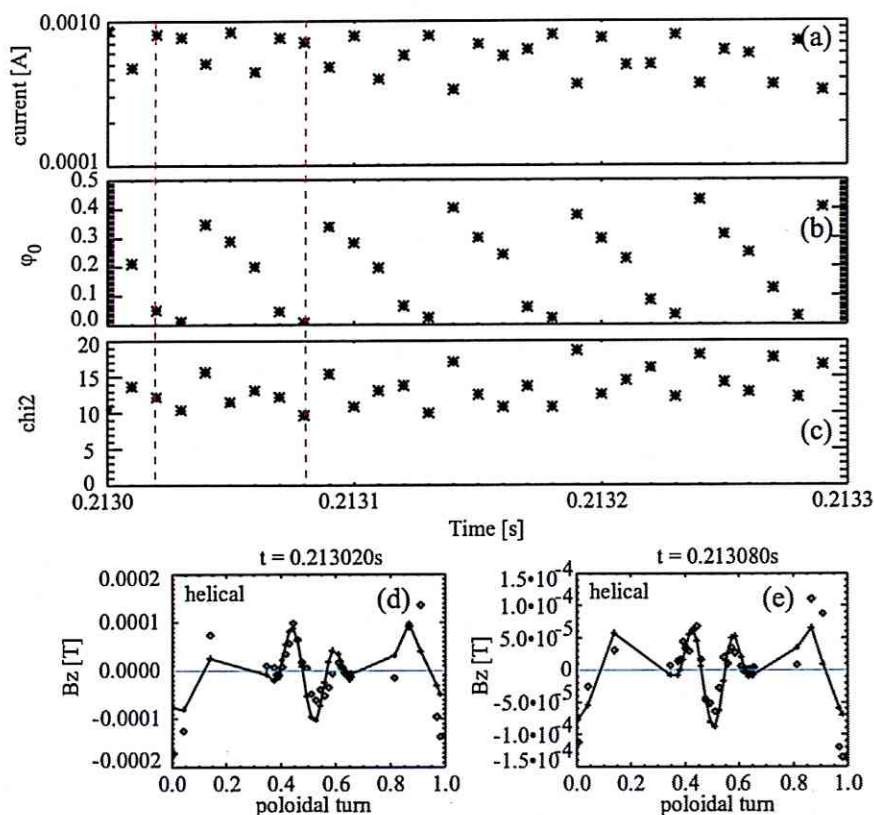


Figure 6.6: Time evolutions of the fitting results by the helical model. (a) Maximum current of filamentary currents [A], (b) toroidal offset angle [turns], (c) χ^2 . Bottom figures show the vertical component of magnetic field (B_z) measured by Mirnov coils and fitted results by helical and axisymmetric models at $t = 0.24231$ s (d, e) and 0.24950 s (f, g) indicated by red dashed lines in the top figure.

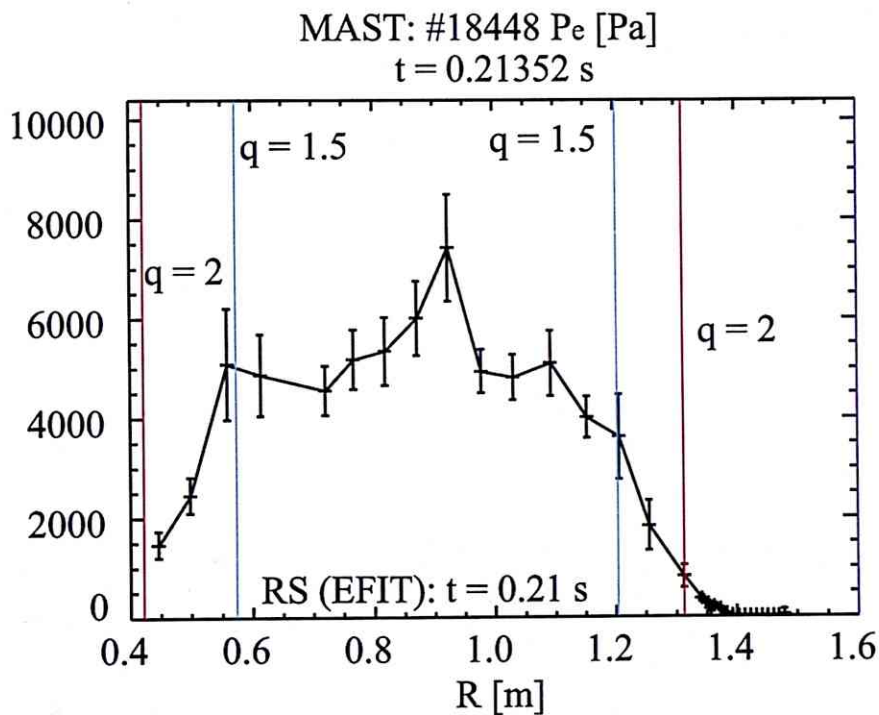


Figure 6.7: Electron pressure profile measured by Thomson scattering at $t = 0.21352$ s. Blue and red vertical lines indicate positions of the rational surfaces at $q = 1.5$ and 2, based on EFIT reconstruction at $t = 0.21$ s.

Chapter 7

MHD instabilities in MAST

7.1 Characteristics of sawtooth oscillation in MAST

In most tokamak experiments sawtooth oscillations are observed. The sawtooth oscillation often involves a growth of $m/n = 1/1$ mode at the $q = 1$ surface followed by a sudden crash of the central density and temperature[99]. When $q_0 \sim 1$ (q_0 is the safety factor at the magnetic axis), the IRE needs to be distinguished from the sawtooth oscillation. Since the $q \sim 1$ surface is usually located nearby the centre of the plasma, the sawtooth collapse occurs just in the core region, and the plasma current does not show an appreciable increase, indicating that a large change of the plasma current profile does not occur. Therefore, the loss of (β) is small, typically less than a few %. On the contrary IREs reduce the plasma pressure and flatten the current density profile, and in some cases even terminates the discharge. Figure 7.1 shows a discharge with at least two sawtooth crashes. The plasma current (I_p) does not change at a sawtooth crash, indicating that the change in the current density profile is small. The SXR profile shows a transport of heat from the core to the edge of the plasma. HCAMU#2-5 intensities decrease at $t = 0.329$ s and HCAMU#6-12 intensities increase at the same timing. The inversion surface, where the change of SXR intensity switches from increase to decrease, is at the $q = 1$ surface.

7.2 Characteristics of IRE on MAST

Figure 7.2 shows waveforms of a typical MAST L-mode discharge with IREs. The plasma parameters are: $I_p \sim 1.1$ MA, $B_t \sim 0.5$ T, $n_e(0) \sim 4 \times 10^{19} \text{ m}^{-3}$,

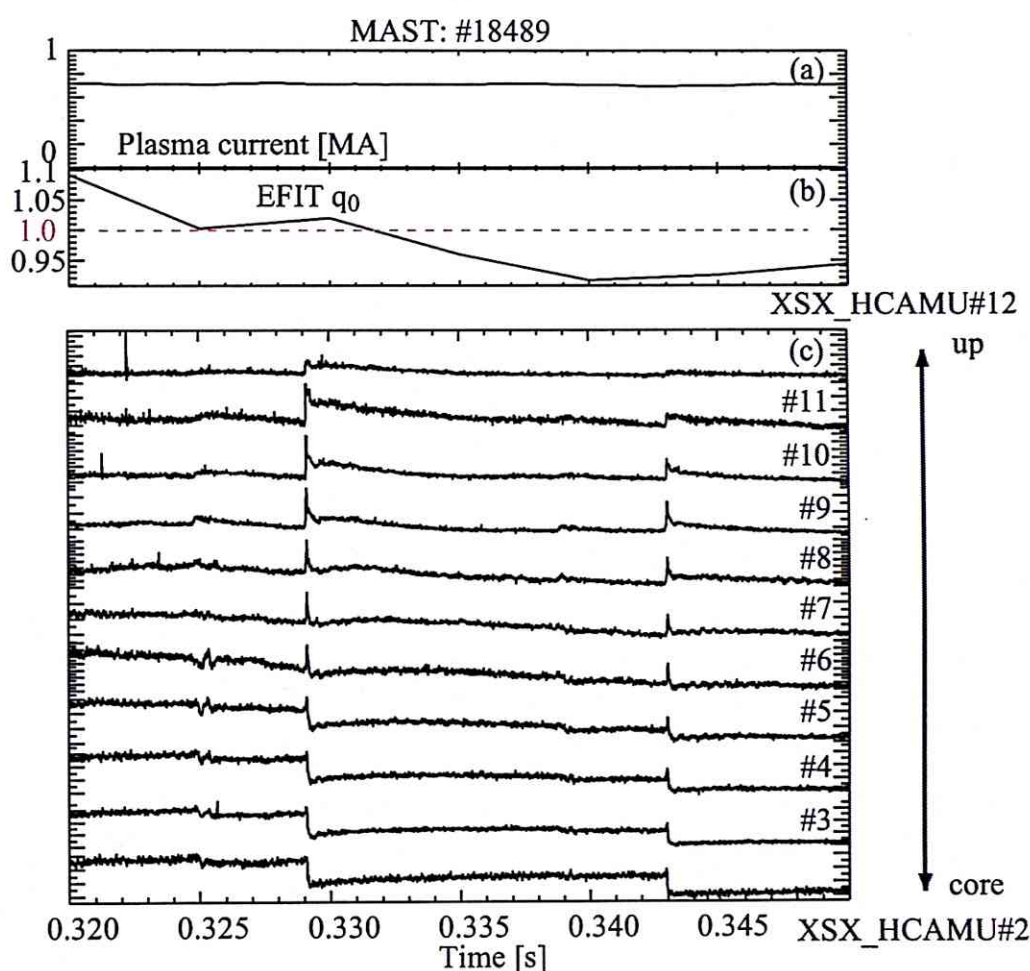


Figure 7.1: Typical MAST discharge with a sawtooth oscillation (#18489). (a) Plasma current [MA], (b) safety factor at the magnetic axis (q_0), (c) SXR radiation measured by the upper horizontal camera [a.u.].

and $P_{NB} = 3.2$ MW. Prior to the major collapse at $t = 229$ ms, we observe a small collapse at $t = 225$ ms. The plasma current shows a large positive spike at $t \sim 0.23$ s due to the reconnection which flattens the current density profile. The line integrated electron density shows a rapid drop during the IRE. The toroidal β calculated by EFIT shows a thermal quench starting at $t = 225$ ms. In order to understand the evolution of the SXR profile and the mode structure, SXR signals of selected channels of the upper horizontal SXR camera HCAMU are shown in Fig. 7.3. An inward propagation of the perturbation (i.e. energy loss) triggered by the small collapse at $t = 225$ ms can be seen. This can be contrasted with a sawtooth crash which propagates from the core to the edge. The small event, which has a clear low- n precursor, was followed by a large collapse starting at $t = 228$ ms. Fluctuations with a frequency of several kHz can be seen on HCAMU#10–16. The position from which the collapse starts is near the edge, but near a rational surface which is identified by the behavior of SXR signals. A tearing mode is localized at a rational surface and creates an island, within which the pressure becomes flattened. When an island rotates along the toroidal or poloidal direction, the local gradient oscillates radially. SXR signals measured on both sides of the island will have opposite phases. Thus, the out-of-phase oscillations between nearby SXR chords indicate the existence of an island at a rational surface.

Figure 7.4 shows dB/dt measured by Mirnov coils located at various toroidal and poloidal locations: toroidal array on the centre column, $R = 0.18$ m, $z = 0$ m, and poloidal arrays on the outboard wall and the centre column. Two modes can be identified in this plot. The slowest mode (~ 4 kHz) is the $m/n = 2/1$ tearing mode which is the same mode as that observed on the SXR profile, HCAMU#10–16. This identification of the mode number was obtained using the fitting code in Chap. 6. The second mode can be seen in the red shaded area. The frequency is ~ 10 kHz and it appears prior to the first small IRE at $t = 225$ ms. From $t \sim 225$ ms, we observe the edge SXR chord signals decrease first, indicating the start of the collapse. Subsequently, the SXR collapse propagates towards the core. This second mode with ~ 30 kHz is more clearly seen in another MAST discharge discussed later.

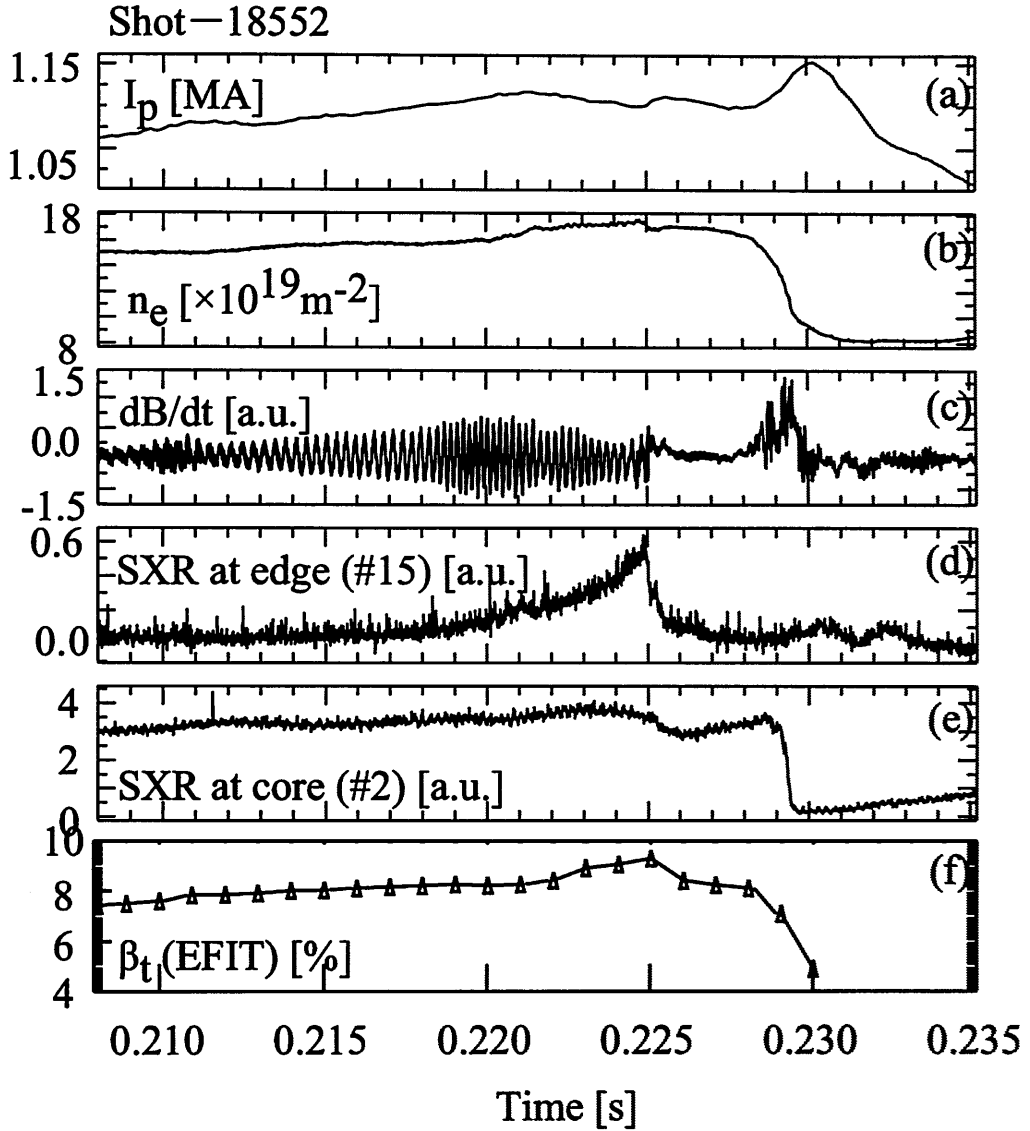


Figure 7.2: Waveforms of a typical MAST L-mode discharge with IREs, with $I_p \sim 1.1$ MA, $B_t \sim 0.5$ T, $n_e(0) \sim 4 \times 10^{19} \text{ m}^{-3}$, $P_{NB} = 3.7$ MW. (a) Plasma current [MA], (b) line integrated electron density [10^{19} m^{-2}], (c) dB/dt [a.u.] measured by the Mirnov coil at $R = 0.18$ m, $z = 0.0$ m, (d), (e) SXR measured along the edge chord #15 ($z = 0.9$ m at $R = 0.7$ m) and the core chord #2 ($z = 0.0$ m at $R = 0.7$ m) of the HCAMU camera [a.u.], and (f) toroidal β calculated by EFIT.

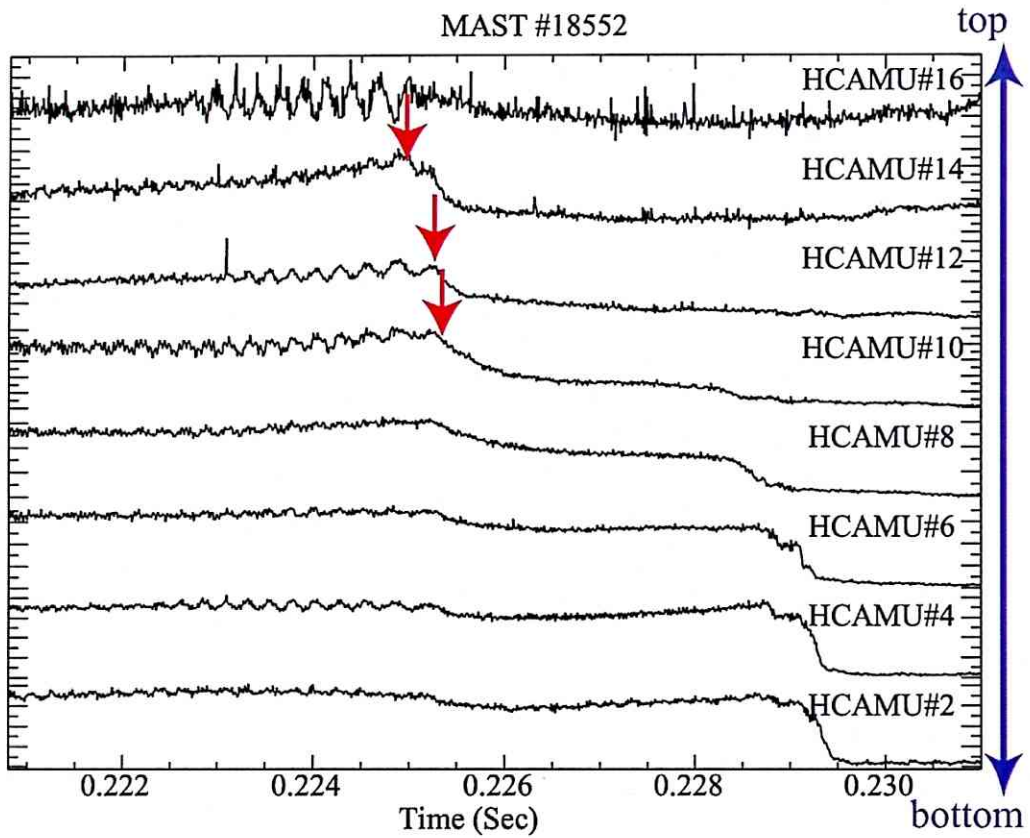


Figure 7.3: SXR waveforms for the same discharge as Fig. 7.2. Several channels from the edge (top chord of HCAMU array) to the core (bottom chord of HCAMU array) are shown. Red arrows indicate the beginning of collapse for each channel.

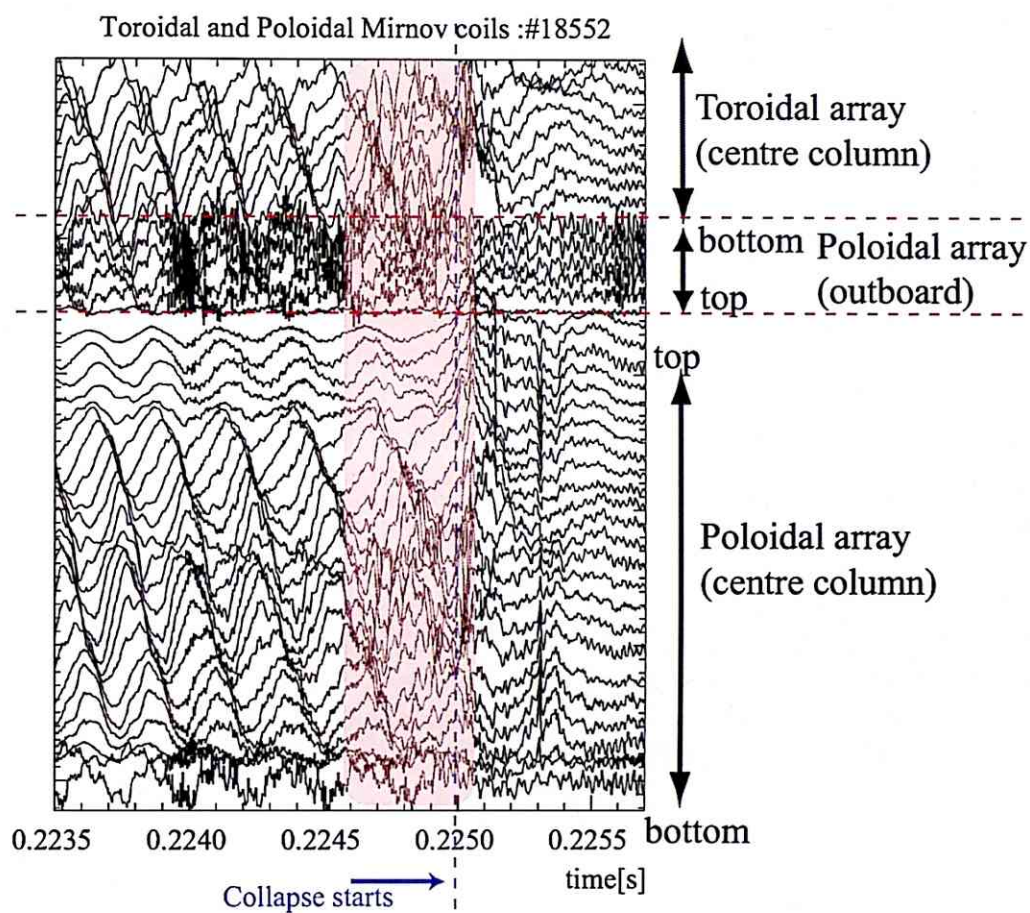


Figure 7.4: Toroidal and poloidal variations of dB/dt measured by Mirnov coils. (#18552)

A similar discharge, but with slightly different collapse behaviour, is discussed below. Figure 7.5 shows discharge waveforms of MAST pulse 18547, with IRE at $t = 250$ ms, L-mode, $I_p \sim 1.1$ MA, $B_t \sim 0.6$ T, $n_e(0) \sim 4 \times 10^{19} \text{ m}^{-3}$, $P_{NB} \sim 3.1$ MW. In this discharge the same type of collapse, starting from the outside of the plasma as in shot #18552, is observed at $t = 249.5$ ms.

Figure 7.6 shows SXR signals measured by the horizontal camera HCAMU from the edge chord (top) to the core chord in MAST pulse #18547. A collapse of the SXR signal starts at $t \sim 0.2495$ s (HCAMU#12), and drops substantially. The decrease in the central SXR chord, HCAMU#2, has a clear delay, starting at $t = 0.252$ s, together with the collapse of the central density shown in Fig. 7.5.

Figure 7.7 shows the toroidal and poloidal variations of dB/dt measured by Mirnov coils, with the same layout as in Fig. 7.4. The collapse of the edge SXR signal starts at $t \sim 0.2495$ s. As in Fig. 7.7, there are at least two different low- n modes. One is the slow (\sim a few kHz), dominant mode identified as the $m/n = 2/1$ mode. The second mode ($n = 2$ with ~ 10 kHz) can be seen in the red shaded area $t = 0.2494$ – 0.2499 s in Fig. 7.7, and is very similar to the mode in the previous shot (#18552). The difference from the previous shot is that the first, small reconnection at $t = 249.5$ ms occurs deeper in the plasma, close to the $q = 2$ surface (a phase inversion is clearly seen). The tearing mode continues to grow for ~ 1 ms, and then either becomes locked, or becomes a global mode. This can be seen on the SXR profile, showing the collapse starting at HCAMU#12, near the $q = 2$ surface. In contrast, the collapse starts from the periphery in the previous shot. In both cases only a small fraction of the plasma thermal energy is lost. Mode coupling occurs in both cases, as seen in Figs. 7.4 and 7.7.

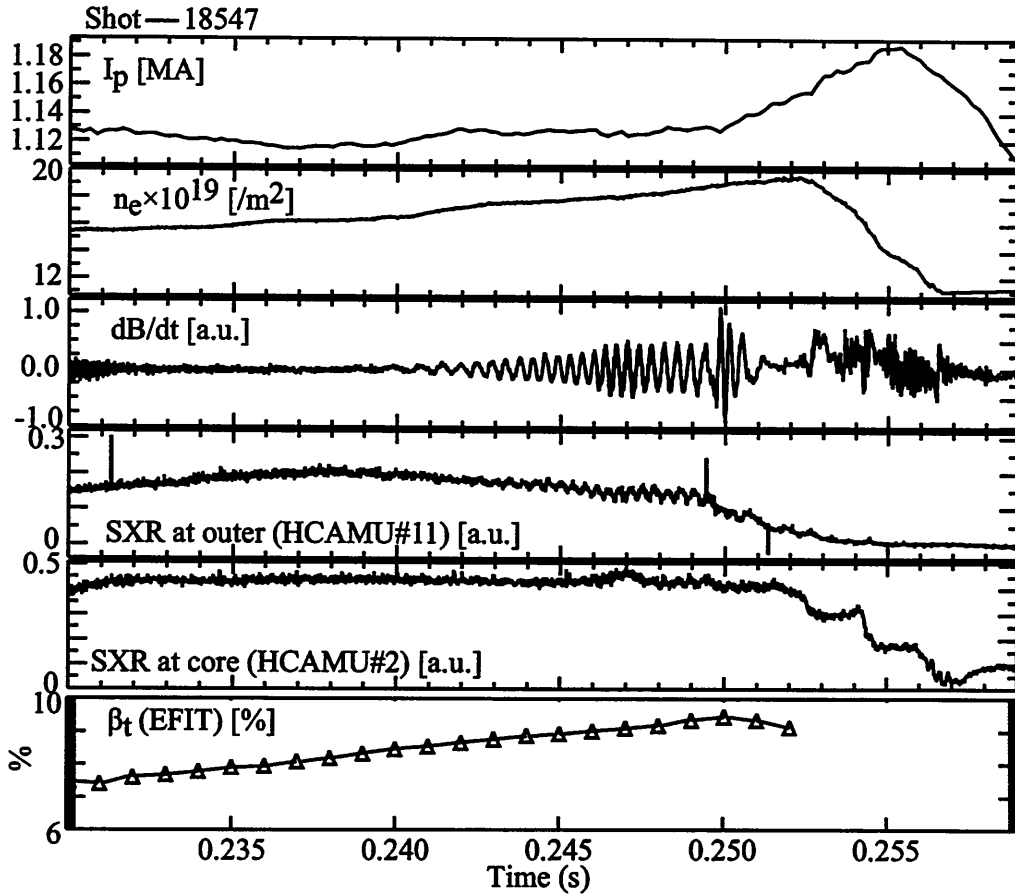


Figure 7.5: MAST discharge with an IRE. L-mode, $I_p \sim 1.1$ MA, $B_t \sim 0.6$ T, $n_e(0) \sim 4 \times 10^{19} \text{ m}^{-3}$, $P_{NB} \sim 3.1$ MW. (a) Plasma current [MA], (b) line integrated electron density [10^{19} m^{-2}], (c) dB/dt measured by the Mirnov coil at $R = 0.18 \text{ m}$, $z = 0 \text{ m}$ [a.u.], (d) and (e) SXR along edge and core chords of HCAMU [a.u.], and (f) toroidal β from EFIT.

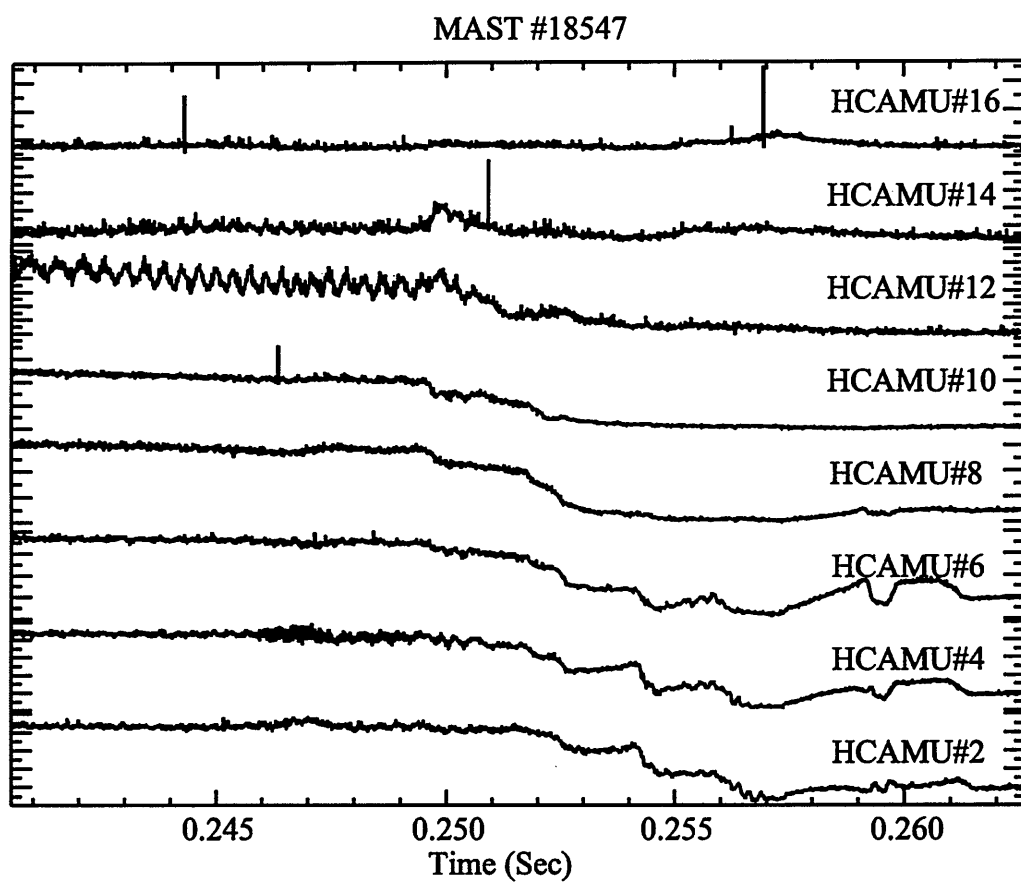


Figure 7.6: HCAMU SXR signals from the edge chord (top) to the core chord measured in MAST pulse #18547.

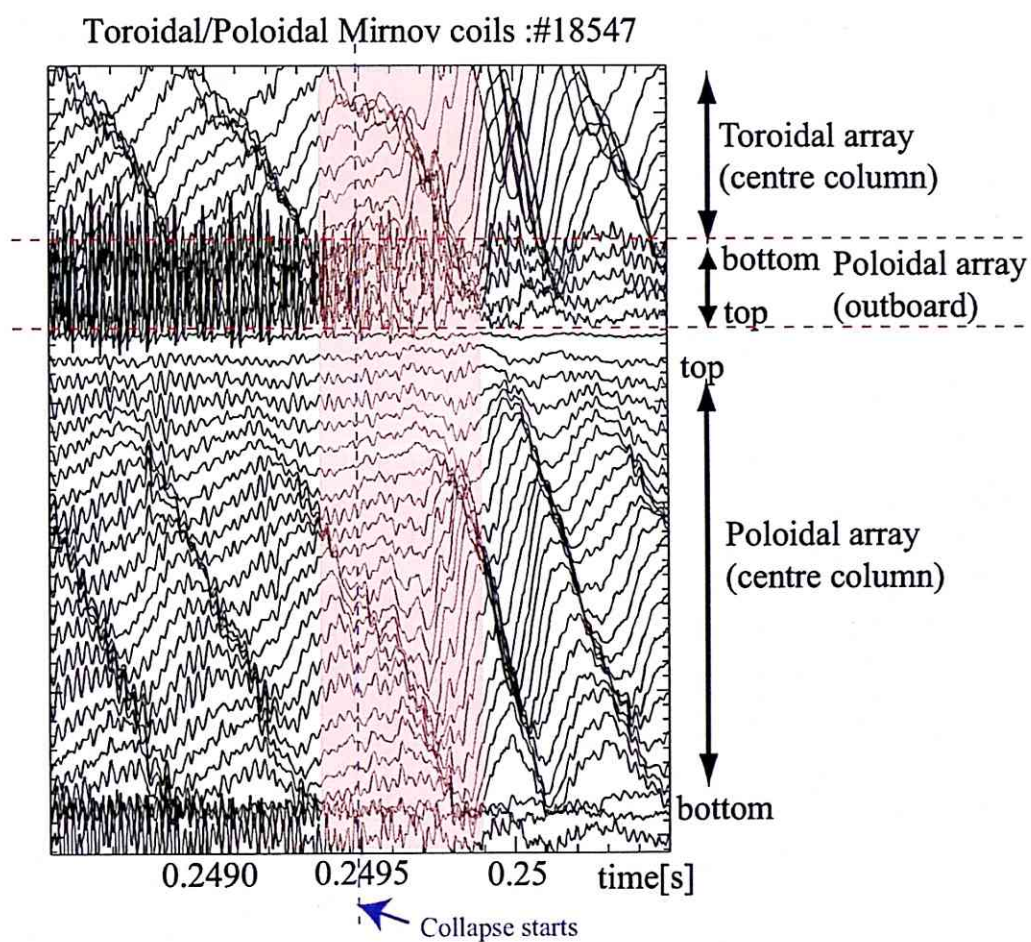


Figure 7.7: dB/dt measured by Mirnov coils in MAST. (#18547)

7.3 Mode analysis with SVD and filamentary models

7.3.1 SVD analysis

In order to understand the precursor mode structure in detail, the SVD method was employed. Signals from not only poloidal Mirnov coils (31 coils) but also from toroidal Mirnov coils (8 coils) were used in order to identify both m and n mode numbers for each coherent mode. Figure 7.8 shows the results of SVD analysis. Note that these signals are not integrated and are band-pass filtered in the frequency range 1–125 kHz. Chrono, topo for poloidal

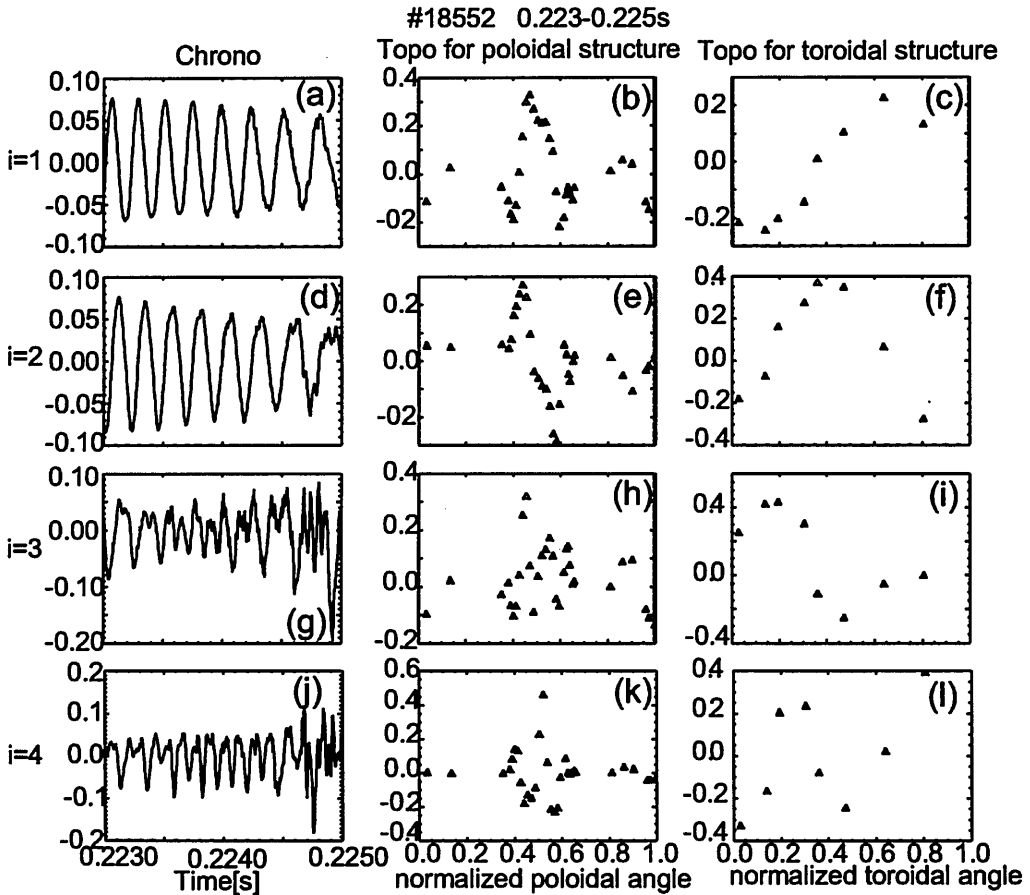


Figure 7.8: (a), (d), (g), (k) Chrono and (b), (e), (h), (k) topo for poloidal Mirnov coils, and (c), (f), (i), (l) topo for toroidal Mirnov coils. The row number indicated by i corresponds to the mode number of SVD analysis.

Mirnov coils, and topo for toroidal Mirnov coils are shown. The four rows correspond to the mode number i labeled by the singular value in descending order, $i = 1$ being the most dominant mode. The first four singular values are $\sigma_1 = 1392$, $\sigma_2 = 1062$, $\sigma_3 = 395$, and $\sigma_4 = 351$ (see Fig. 7.9). For modes

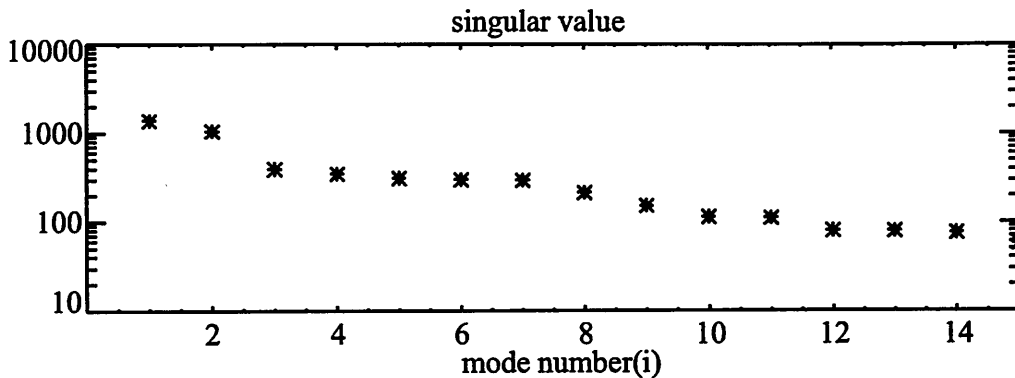


Figure 7.9: Singular values obtained by SVD analysis for $t = 0.223\text{--}0.225$ s.

$i = 1$ and 2, the powers (i.e., the singular values) are almost the same, and the phase difference between the two modes is about 90° , indicating a rotating mode. The poloidal and toroidal mode numbers were identified using the elementary code described in Chap. 6. Figure 7.10 shows the results of the fit assuming the $m/n = 2/1$ mode for topois in Fig. 7.8. (a) and (b) are topois of the poloidal structure for $i = 1$ and 2, respectively. Other mode numbers, $m/n = 1/1$, $3/2$, and $3/1$, were also tried for mode number identification. The $m/n = 2/1$ mode showed the minimum residual error. Therefore, the dominant mode shown in Fig. 7.10 is identified as the $2/1$ mode. The toroidal mode ($n = 1$) is also confirmed by the topo waveform in Fig. 7.8 (c) and (f), showing one period along the toroidal circumference. For $i = 3$ and 4, the time evolutions of chronos from $t = 0.2245$ s are similar to the precursor during the red shaded period in Fig. 7.4. These toroidal structures are dominated by $n = 2$, as can be seen in Fig. 7.8(l). However, the poloidal structure indicates complicated waveforms ($m > 4$, presumably). This may be due to a non-linear coupling. The appearance of the $n = 1$ and $n = 2$ modes has a similarity to Case 3 of the simulation result shown in Fig. 2.15, in which some low- n modes show significant growths earlier than high- n modes.

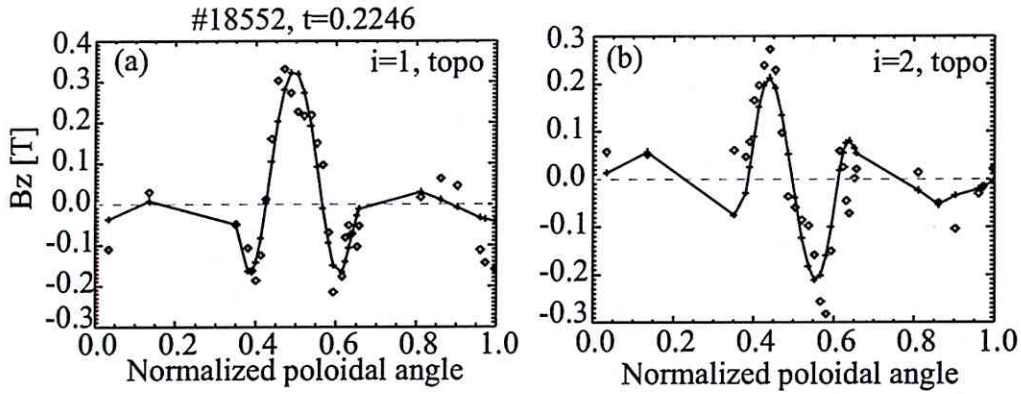


Figure 7.10: Fitting results assuming the $m/n = 2/1$ mode for topos in Fig. 7.8. (a) and (b) are topo of the poloidal structure for $i = 1$ and 2, respectively.

7.3.2 Filamentary models for understanding complicated mode structures

In order to identify the mode number ($m > 4$ precursor just before the collapse), analyses using filamentary models were executed. It is not easy to extract a complicated and weak mode from the signals of Mirnov coils. For a single mode, assuming that there is one dominant mode, the filamentary model is very effective for reconstructing the mode structure. As described in Sec. 6, it finds suitable mode numbers and tries to obtain the time evolution. For multi modes, there are two methods to determine the mode numbers and their structures. One method uses the Fourier analysis and extracts the high power components in frequency space. However, the waveforms of magnetic fluctuations have various frequency components, and it is not suitable to apply this method. The other method uses subtraction without the Fourier analysis. It subtracts the single mode result for lower mode numbers from the measured magnetic fluctuation data, and uses the single mode method again for higher mode numbers. This is called the multi mode method. The results of fitting using $m/n = 2/1$ and $m/n = 5/2$ modes at two different times are shown in Fig. 7.11. The results indicate the co-existence of two modes just before IRE, suggesting a mode coupling of the two modes. After that, a collapse and strong magnetic fluctuations occur (within $\sim 300 \mu\text{s}$). From the point of view of poloidal structure of magnetic fluctuations, the mode coupling between $m/n = 2/1$ and $m/n = 5/2$ modes is shown. When the rotation shear between the two modes is not so significant and the phase relation tend to be constant, positive or negative components

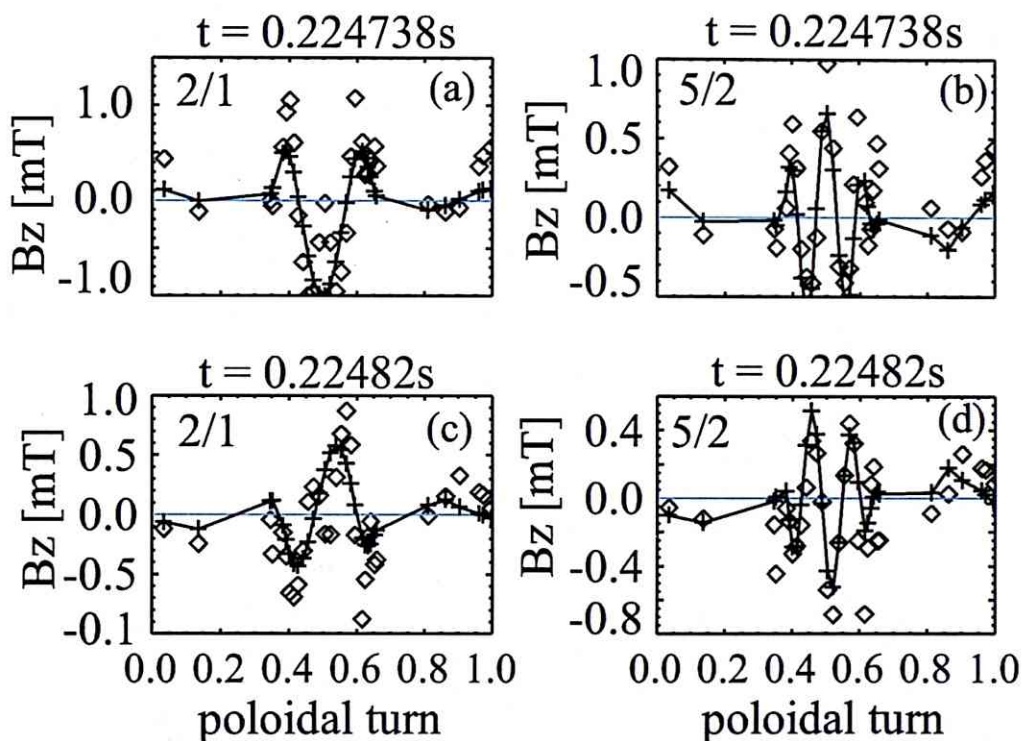


Figure 7.11: Fitting results assuming $m/n = 2/1$ and $5/2$ modes at (a), (b) $t = 0.224738\text{s}$ and (c), (d) $t = 0.22482\text{s}$. The $5/2$ mode fitting was performed after subtracting the $2/1$ mode fitting result.

of the two modes strengthen each other, and leads to a large deformation of the magnetic surface. This is the phase alignment and is also observed in the TST-2 plasma (see Sec. 4.3.1) . For example, both modes show negative components of magnetic field at $\theta \sim 0.4$ in Fig. 7.11(c), (d).

7.4 Collapses with locked and ballooning mode

Collapses with the ballooning mode were confirmed experimentally in the TFTR tokamak (see Sec. 2.2). The ballooning mode has a high- n structure localized on the low field side in a region with steep pressure gradient. Since the frequency of magnetic fluctuation is determined by the plasma rotation and is multiplied by n in the usual case with dominantly toroidal rotation, it is observed as a high-frequency magnetic fluctuation. Collapse events with a high frequency mode and without a tearing mode have been confirmed in MAST discharges.

Figure 7.12 shows a MAST H-mode discharge with a locked mode from $t = 0.267$ s, with $I_p \sim 0.8$ MA, $B_t \sim 0.6$ T, $n_e(0) \sim 4 \times 10^{19} \text{ m}^{-3}$, and $P_{NB} \sim 3.1$ MW. The plasma current shows an increase after $t \sim 0.2675$ s, whereas the line integrated electron density shows a rapid decrease. The magnetic fluctuation measured by the Mirnov coil at $R = 1.8$ m, $z = 0$ m shows a slow (5 kHz) $n = 1$ mode and a high (~ 100 kHz) frequency mode just before the collapse. SXR measured by the horizontal camera indicates a slowing down of mode rotation leading to mode locking. SXR intensity increases rapidly after mode locking, and a high frequency mode becomes visible before the collapse. The measurement of the SXR profile is effective for determining the location of the high frequency mode,

Figure 7.13 presents SXR radiation given by the horizontal camera. A kink-type mode with $n = 1$, identified by the toroidal Mirnov coil array, appears in the core. At $t \sim 0.2668$ s, the mode locks (stops rotating). Subsequently, a high frequency mode appears from $t \sim 0.2676$ s (red shaded area), but the locked $n = 1$ mode still exists until at least $t = 0.2678$ s. After the appearance of the high-frequency mode, a decrease is observed in SXR in the interior of the plasma (HCAM#5–9, $z > 0.43$ m at $R = 0.7$ m) and an increase in SXR can be seen in outer channels (HCAM#10–12, $z > 0.5$ m at $r = 0.7$ m). Generally, modes with high frequencies have high toroidal mode numbers which are characteristic of pressure driven modes such as the ballooning mode. Note that we do not always observe such high frequency modes, suggesting that these modes may be localized toroidally. Ballooning modes have not been identified clearly in the two previous cases, but are clearly seen in the locked mode case. The locked mode has $n = 1$ and its frequency decreases with time. This difference can be attributed either to the coupling between high- n and low- n modes during mode growth, or to the enhancement of local pressure gradient by the large locked low- n deformation. If the mode with ~ 100 kHz is a pressure driven ballooning mode, there should be a clear difference between the outboard and the inboard fluctuations. Figure 7.14 shows the averaged power spectrum of magnetic

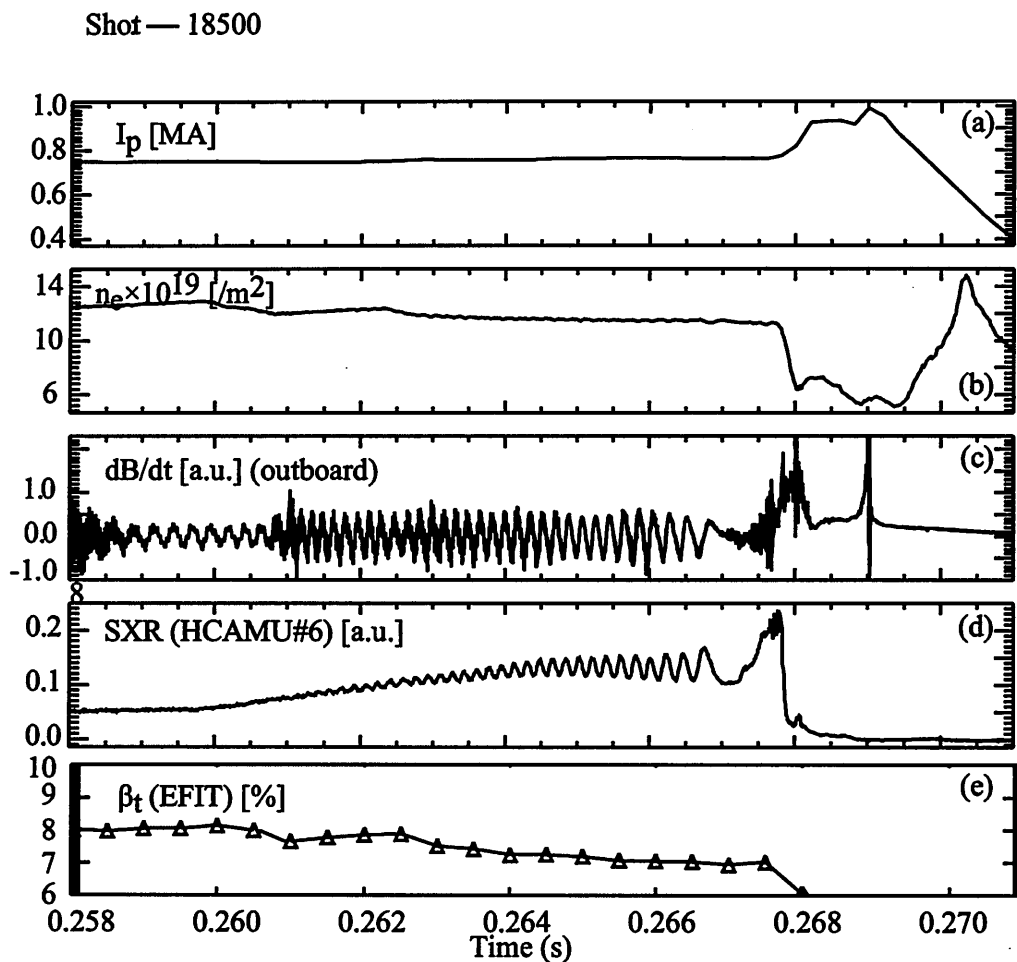


Figure 7.12: MAST pulse with a locked mode. H-mode discharge, $I_p \sim 0.8$ MA, $B_t \sim 0.6$ T, $n_e(0) \sim 4 \times 10^{19} \text{ m}^{-3}$, $P_{NB} \sim 3.1$ MW. (a) Plasma current [MA], (b) line integrated electron density [m^{-2}], (c) dB/dt measured by Mirnov coil [a.u.], (d), (e) SXR at $z \sim 0.24$ m [a.u.], (f) toroidal beta from EFIT reconstruction.

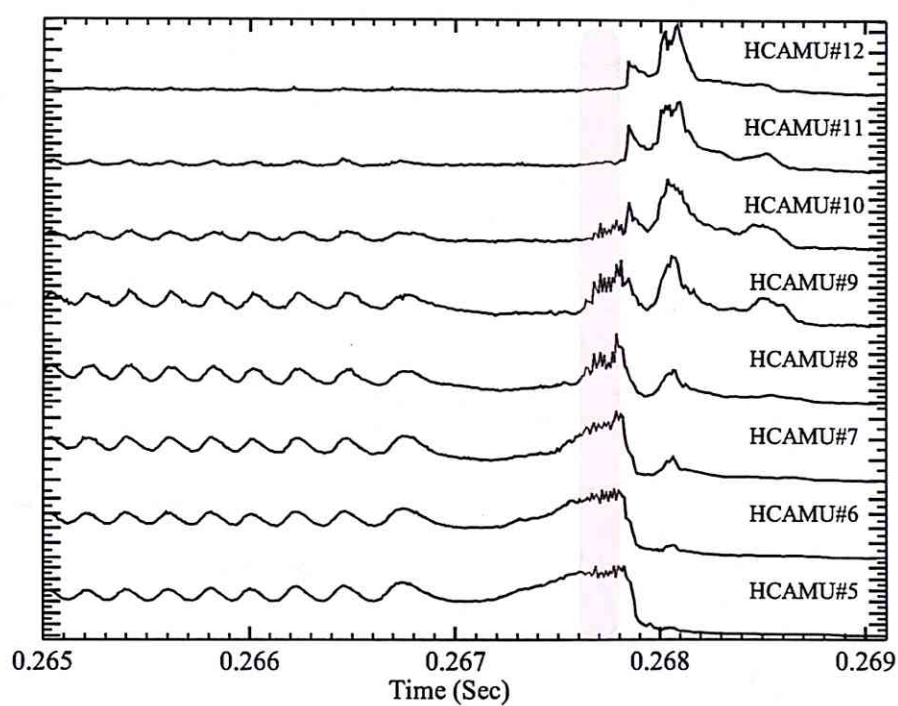


Figure 7.13: Expanded view of the SXR signals measured by the horizontal camera. Red shaded area ($t = 0.2676\text{--}0.2678\text{ s}$) indicates the period with a high frequency mode.

fluctuations on the inboard side (Ch. 8) and on the outboard side (Ch. 3), indicating a pressure driven character. Note that the amplitude is corrected

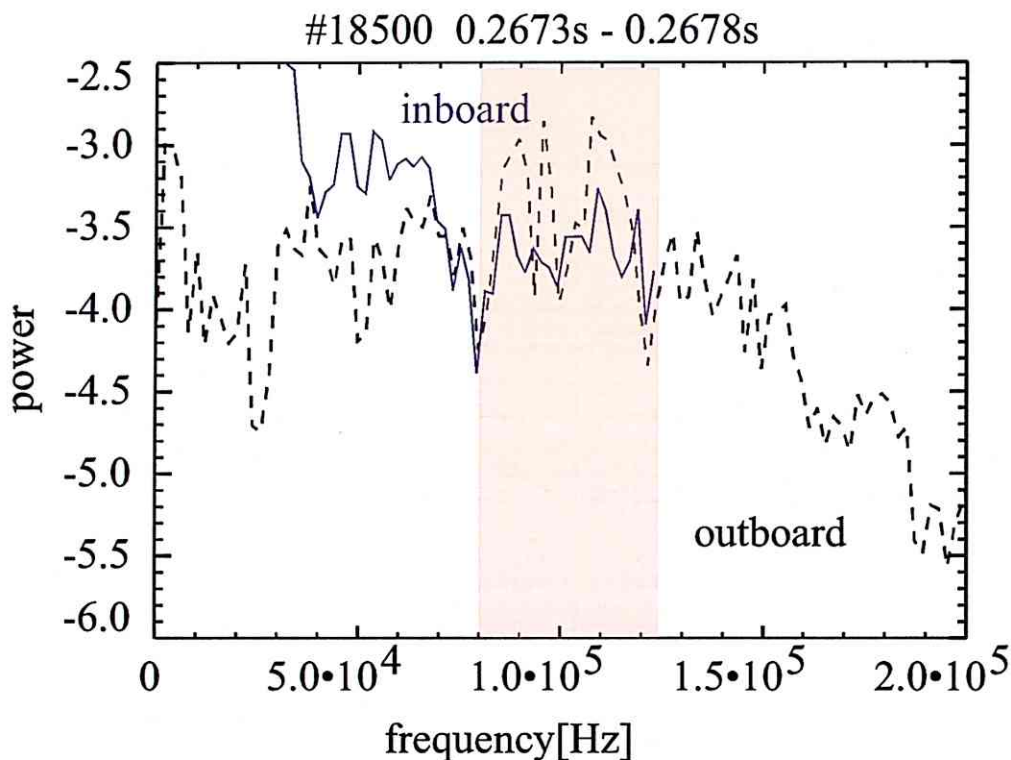


Figure 7.14: Averaged magnetic fluctuation power spectrum on the inboard side (Ch. 8) and on the outboard side (Ch. 3) on the logarithmic scale. The signals are normalized by the distance between the magnetic axis and the position of each coil.

by a factor inversely proportional to the distance between the magnetic axis and positions of each coil to compensate for the distance effect. The power on the outboard side at ~ 100 kHz is greater by the factor of ~ 10 . Therefore we conclude that the mode is localized on the outboard side. In order to identify the mode number, the cross correlation analysis is very useful because the toroidal mode number can be determined from the phase difference when coherence is high. Figure 7.15 shows the results of the cross spectrum analysis using two OMAHA coils at toroidal angles $\phi = 267.5^\circ$ and 277.5° . The cross-coherence is nearly 1 for $70 < f < 130$ kHz, and the cross phase is $40 - -70^\circ$, indicating a toroidal mode number of up to $n \sim 7$, because the two coils are separated by $10 \circ$ toroidally.

Figure 7.16 shows the electron pressure profiles measured by the YAG

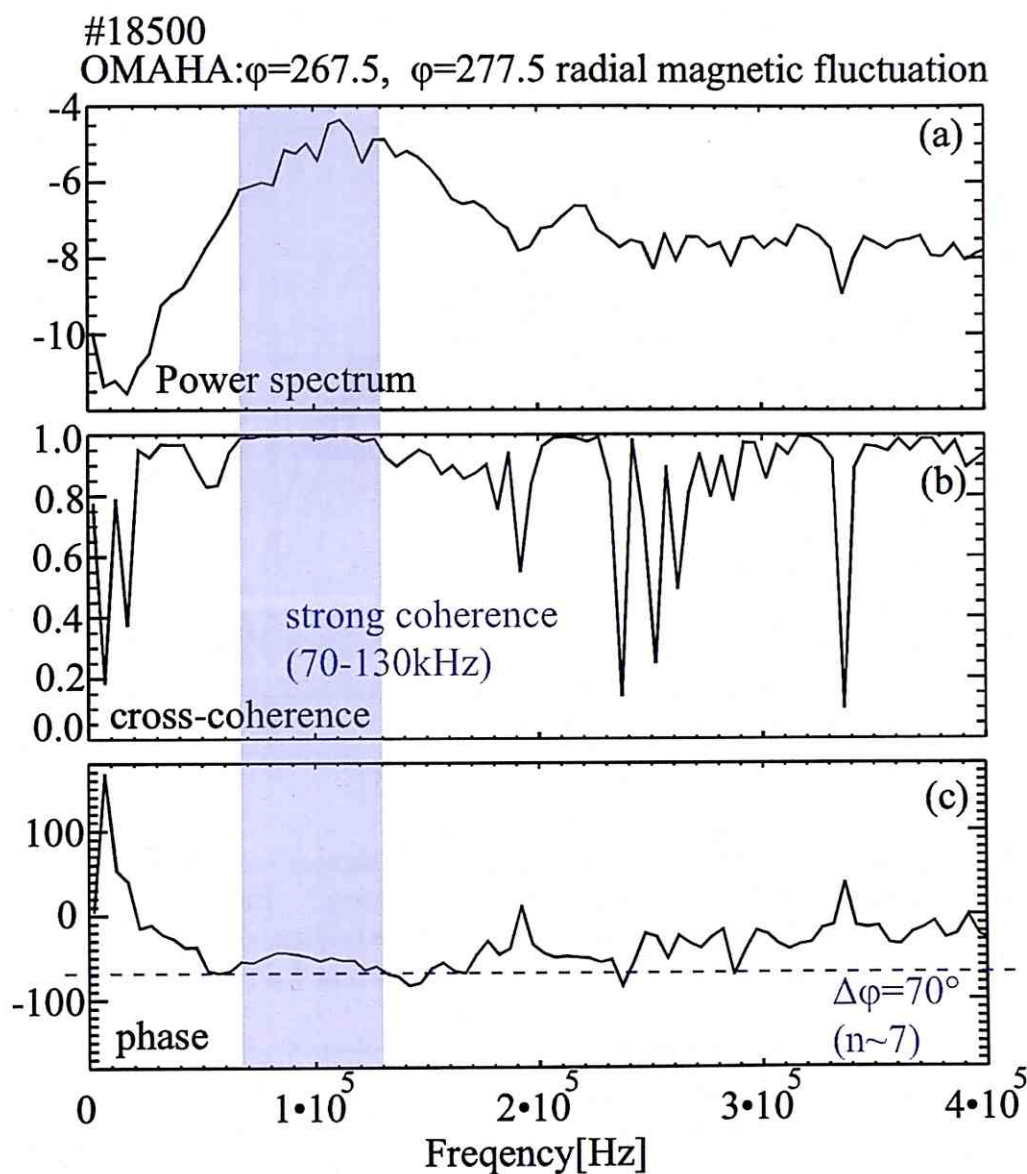


Figure 7.15: Results of cross spectrum analysis using two OMAHA coils at $\phi = 267.5^\circ$ and 277.5° . (a) Power spectrum, (b) cross-coherence, and (c) cross phase.

laser Thomson scattering system at $t = 0.2561$ s (black), 0.2611 s (blue), and 0.2661 s (green). Radial positions of rational surfaces (RS) obtained by EFIT reconstruction at $t = 0.265$ s are also plotted. At $t = 0.2661$ s,

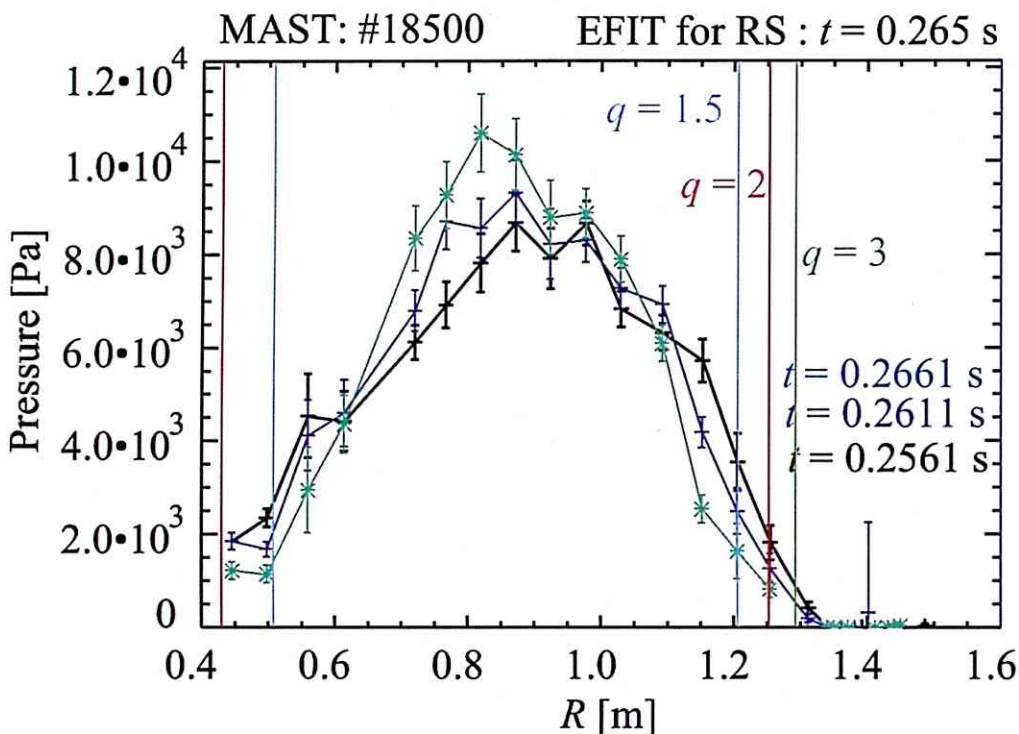


Figure 7.16: Pressure profiles measured by Thomson scattering at $t = 0.2561$ s (black), 0.2611 s (blue), and 0.2661 s (green). Radial positions of rational surfaces (RS) obtained by EFIT reconstruction at $t = 0.265$ s are also shown by the light blue ($q = 1.5$), red ($q = 2$), and green ($q = 3$) lines.

which is 0.7 ms before the collapse, the pressure profile is steep in the core of the plasma ($R = 0.6$ – 1.2 m). The maximum pressure gradient estimated by a polynomial fit increases from 3.1×10^4 Pa/m at $t = 0.2561$ s to 4.0×10^4 Pa/m at $t = 0.2661$ s. The increase in the pressure gradient before the IRE is a possible cause of the ballooning mode. Moreover, at $t = 0.2661$ s the region with steep pressure gradient is $1.0 < R < 1.2$ m, while the horizontal SXR camera data in Fig. 7.13 shows that the high frequency mode exists for $R < 1.2$ m, where the radial position was determined from EFIT (see Sec. 5.2.5). Therefore, this mode satisfies the conditions of the pressure driven ballooning mode. In order to evaluate the threshold pressure gradient, three shots with different behaviours are compared in Fig. 7.17. These shots

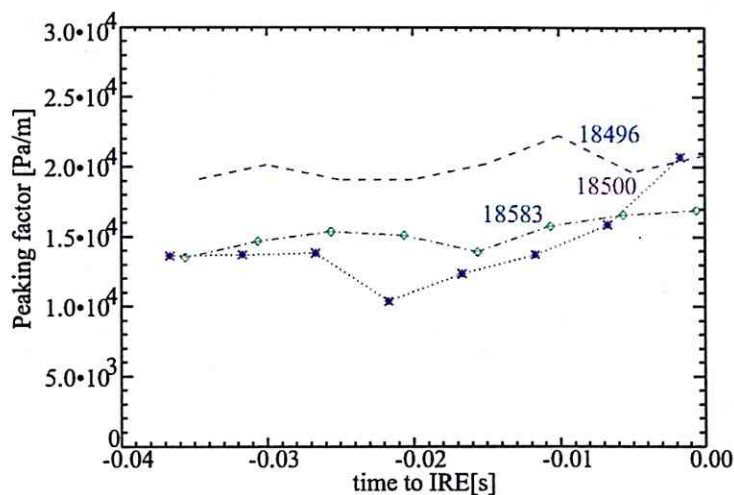


Figure 7.17: Time evolutions of the electron pressure profile peaking factor determined from the TS data.

have the internal mode, the locked mode ($m = \text{odd}$), and an increase of the maximum pressure gradient before IRE, as in #18500. The threshold is $\sim 2 \times 10^4$ Pa/m. We conclude that maximum pressure gradient must be kept $< 2 \times 10^4$ Pa/m for avoiding IRE.

7.5 Stability analysis with kEFIT

The ballooning mode discussed in the previous section is clearly a pressure driven mode. However, IREs accompanying non-linear mode coupling and/or propagation of SXR decrease from the outside to the core region require a stability analysis in terms of current density profile and pressure profile, because it is necessary to understand the stability limit to prevent the occurrence of IRE. Figure 7.18 shows trajectories of the magnetic shear (S) and the pressure gradient (dP/dr) for thirteen shots, where magnetic shear is defined as

$$S = \frac{r}{q} \cdot \frac{dq}{dr}. \quad (7.1)$$

These two parameters are calculated by kEFIT (see Sec. 5.2.4) which takes

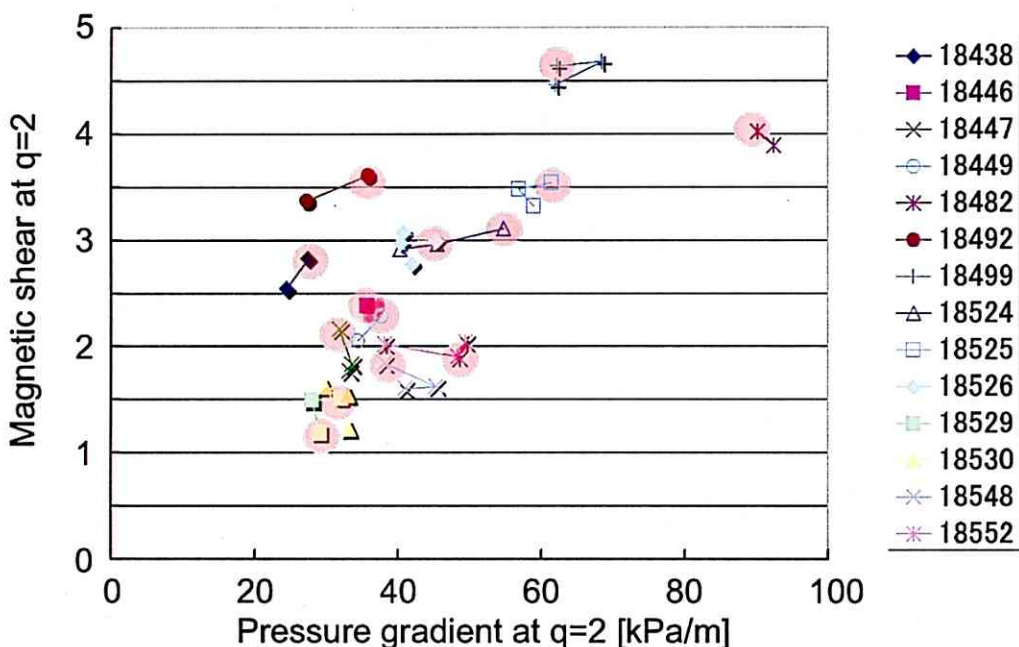


Figure 7.18: Trajectories of magnetic shear (S) and pressure gradient at the $q = 2$ surface before ($0 \sim 21$ ms) an IRE, based on kEFIT analysis. Same symbol show the same shot. The red shaded circles indicate times just before IRE.

into account the electron pressure profile measured by Thomson scattering. Red circles represent the values just before each IRE. IRE occurs when the pressure gradient exceeds a critical value, which increases at high shear, indicating the stabilizing effect of magnetic shear. Note that although many

shots show an increase of the pressure gradient before IRE, some shots do not show such a behavior. Therefore, it is possible that another hidden parameter triggers an IRE.

Chapter 8

Discussion and Conclusions

8.1 IREs in MAST

8.1.1 Coupling of multiple low- n modes

The first examples of IRE (#18552 and #18547) show the co-existence of two modes before and during the collapse. By using the three dimensional (helical) filamentary model, it was confirmed that magnetic fluctuations from $m/n = 5/2$ and $2/1$ modes are coupled to each other. The model assumes that the modes are localized at corresponding resonant rational surfaces. The $2/1$ tearing mode was identified clearly from the time evolution of SXR profile. One type (#18552) shows an appearance of the $m/n = 5/2$ mode $\sim 400 \mu\text{s}$ before the collapse. The position where the collapse starts, as determined from the SXR profile, is near the edge, close to the $q = 2$ surface. In the other type (#18547), the $m/n = 3/2$ mode identified by the filamentary model appears almost at the same time as the beginning of the collapse. The collapse starts from inside the $q = 2$ surface. The difference in the region of collapse is presumably responsible for the different behaviour. Time evolutions of these modes ($n = 1$ and 2) are very similar, as shown in Fig. 8.1. The mode energies are calculated from the inboard Mirnov coil data and are normalized by the time averaged vertical magnetic field energy. In #18547, by the time collapse starts near the $q = 2$ surface (indicated by the red triangle), $n = \text{odd}$ and $n = \text{even}$ components reach the largest energies just before the IRE. In #18552, the $n = \text{odd}$ component reaches the largest energy ($\sim 3 \times 10^{-6}$) before the collapse, but the $n = \text{even}$ component grows suddenly, indicated by the green arrow in Fig. 8.1(c), until it reaches almost the same energy as the $n = \text{odd}$ component. In many other pulses, both $n = \text{odd}$ and even components reach the largest energies at the beginning of an IRE collapse, indicating that the co-existence and coupling of low- n modes

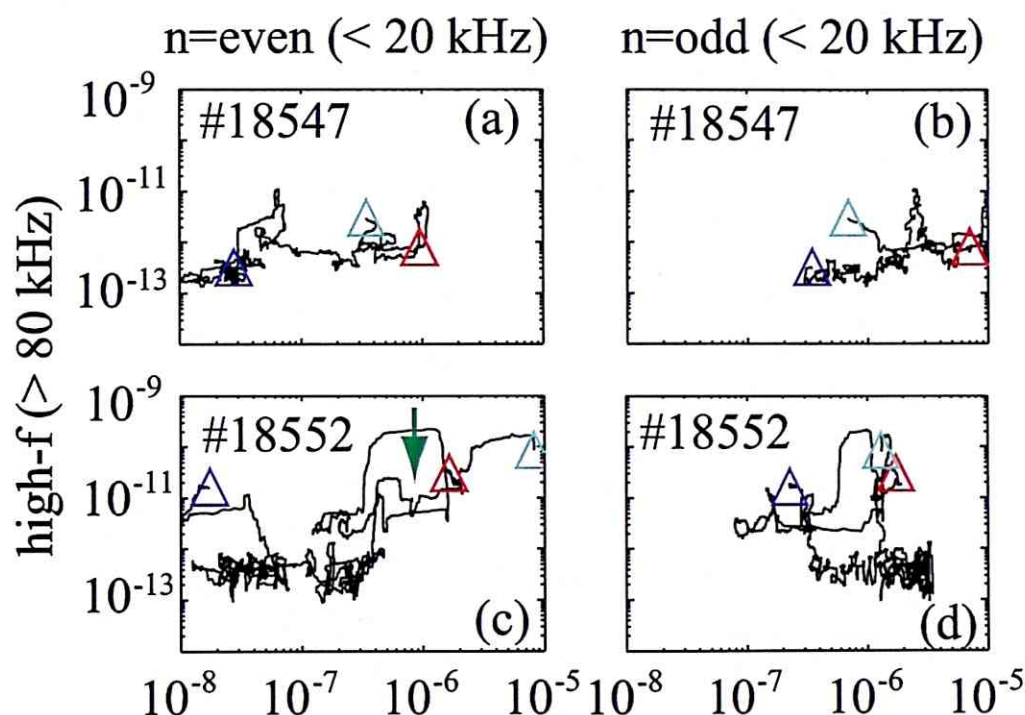


Figure 8.1: Time evolutions of the precursor energy. Horizontal axes are $n = \text{even}$ and $n = \text{odd} (< 20 \text{ kHz})$ energy and vertical axes are the high- f mode ($< 20 \text{ kHz}$) energy. The energies are normalized by the time averaged vertical magnetic field energy. Colored triangles show the initial time (blue), beginning of collapse near the $q = 2$ surface (red), and collapse in the plasma core (light blue).

are essential for triggering an IRE. When modes with sufficiently large intensities overlap with each other (phase alignment), significant deformations of flux surfaces occur. The high- f modes, which are believed to be high- n modes, are observed before the collapse. However, in these two cases there is no correlation between the high- f and low- n ($n = \text{odd and even}$) components. If they were correlated, trajectories of the low- n and high- f energies should change at the same time so that the sum of the mode energies is conserved. Presumably, such high- f modes originate from instabilities driven by energetic particles and are localized in a different region from where the collapse begins. Signs of such high- f mode can be seen weakly on the SXR profile, as on HCAMU#4 in Fig. 7.6.

Turning now to comparison with the results of numerical simulation performed by Hayashi et al. described in Sec. 2.1.5, precursors of IRE reported in this thesis grow much more slowly than those found in the simulation. For MAST parameters, the Alfvén time is approximately $1\ \mu\text{s}$, so the growth time in the simulation ($\sim 10\ \mu\text{s}$) is much shorter than the experimentally observed time scale. Experimentally, the time constants of the $n = 1$ tearing mode and the $n = 2$ mode are approximately 2 ms and a few hundred μs , respectively. However, in terms of mode evolution, there are similarities. The growth of low- n modes ($n = 1$ and 2) predicted in the simulation (Cases 1 and 3 in Fig. 2.15) are observed experimentally. In many cases, the collapse starts when both $n = \text{odd}$ and $n = \text{even}$ components become large, as if there were limits on low- n mode energies. The co-existence of large-amplitude low- n modes suggests coupling and phase alignment between these modes, leading to a local deformation of the flux surface. The simulation shows a localized deformation caused by overlapping of $n = 1$ and 2 modes. The appearance of high- n (high- f) modes is observed in both simulation and experiment. In the simulation high- n modes are excited by harmonic generation from low- n modes, and show the characteristics of ballooning instability. On the other hand, in these two pulses it seems that there is no clear correlation between high- n and low- n modes, because there is no evidence of energy transfer between these modes

8.1.2 Pressure driven ballooning mode

In a locked mode type IRE, the $n = 1$ mode and a steepened pressure gradient are observed. When mode rotation locks, the high-frequency mode localized at the heat bulge created by the $n = 1$ mode appears. A cross spectrum analysis reveals that this mode has a high toroidal mode number ($n < 7$). The magnetic fluctuation intensity normalized by the distance from the magnetic axis to the Mirnov coil is strong on the outboard side. The mode is localized in the region with steep electron pressure gradient. Based on these analyses, the mode is identified as the pressure driven ballooning mode. Unfortunately, the ballooning structure cannot be seen on the SXR profile clearly because the sampling rate of ADC (digitizer) for the SXR camera was 100 kHz. The sampling rate must be at least 200 kHz to see such a structure. The mode numbers and time evolution are very similar between the analysis results and the prediction of simulation (Fig. 2.15) except for the growth rate. The growth rate of the $n = 5$ mode in the simulation corresponds to $\tau = 10 \mu\text{s}$, whereas in the experiment $\tau \sim 100 \mu\text{s}$ is observed by OHAMA coils, including many toroidal numbers. In an experiment on TFTR (a large conventional tokamak), the growth rate of high- n magnetic perturbation is less than $50 \mu\text{s}$. A low- n mode, such as the $m/n = 3/2$ mode is followed by high frequency modes ($n = 7$). In terms of mode numbers (low- n followed by high- n appearing in both results), there is similarity with MAST results. As this kind of instability is pressure driven, it is necessary to avoid a highly peaked pressure profile to prevent this type of IRE.

8.1.3 Comparison with other instabilities: ELM and sawtooth oscillation

As discussed in Sec. 7.1, IREs accompany a clear increase (spike) of plasma current, reflecting a major flattening of the plasma current density profile. In contrast, current spikes are not observed at a sawtooth crash which involves reconnection in the plasma core. A sawtooth crash occurs from the $q \sim 1$ surface whereas an IRE collapse occurs from the $q \sim 2$ surface, and there is a clear difference in the time evolution of profiles.

In the edge region, there is another instability called ELM. (see Sec. 1.2.9). ELMs are triggered by pressure driven modes which occur near the edge region where the pressure gradient becomes very steep in the H-mode. For example the Type I ELM erodes the edge pedestal and affects the region as far inside as $\rho \leq 0.8$. In terms of mode analysis, the difference between IRE and ELM is absolutely clear. Although sometimes IRE accompanies high- n precursors similar to ELM, IRE always accompanies low- n modes. In MAST,

$m/n = 2/1$ and $3/2$ modes are dominant before IRE as precursors.

8.2 IREs in TST-2

In TST-2, large amplitude modes in the core are observed in Ohmic discharges, and the collapse occurs in the core of the plasma, $\rho \sim 0.2$. An increase of ion temperature (measured by line broadening of an OV line emission) is observed just after the beginning of collapse ($\sim 20\mu\text{s}$) suggesting the occurrence of magnetic reconnection. The mode profile is discussed based on Fourier and SVD analyses. Co-existence and phase alignment of $n = 1$ and $n = 2$ modes localized near the collapse location are confirmed. The phase relation between the two modes remain constant so the modes are coupled to each other and the local deformation is observed to increase on the SXR profile. Although the electron temperature in TST-2 ($T_e \sim 100\text{ eV}$) is much lower than in MAST ($T_e \sim 1\text{ keV}$) so the plasma resistivity is much higher, the mode numbers of dominant IRE precursors are the same as in MAST.

8.3 Classification of MHD instabilities

MHD instabilities in ST plasmas can be classified as shown in Fig. 8.2. IRE that accompany low- n modes (especially $n = 1$ and $n = 2$) and a collapse in the internal region of the plasma should be distinguished from sawtooth oscillation and ELM. ELMs are localized at the edge of the plasma $0.8 < \rho < 1$. Sawtooth oscillation with small collapses occur at $q \sim 1$. IRE literally means internal reconnection event, so sawtooth oscillation could be included.

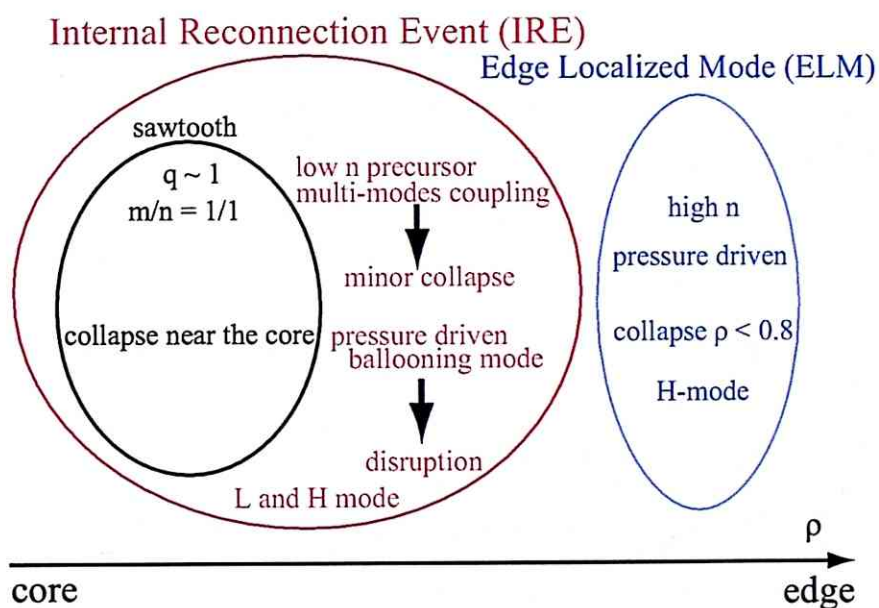


Figure 8.2: Classification of MHD instabilities (IRE, ELM and sawtooth) in ST by the radial position of the collapse

8.4 Conclusions

This work focused on understanding the mechanism that triggers the IRE collapse, as a first step towards realizing stable IRE-free plasmas. In particular, features of the IRE have been investigated experimentally in TST-2 and MAST plasmas with different parameters (such as resistivity) by detailed mode and profile analyses, and were compared with the results of numerical simulation. This thesis suggests ways to avoid some types of IRE. These suggestions may be demonstrated in ST experiments as the next step. The following conclusions can be drawn.

1. In MAST plasmas there are at least two types of IREs which accompany an I_p increase. One has mode coupling between $m/n = 2/1$ and $n = 2$ ($m = 5$ or 3) modes. The other is a pressure driven ballooning mode followed by an $n = 1$ locked mode.
2. IREs show dependences on pressure gradient and magnetic shear. Therefore, it should be possible to avoid these IREs with adequate parameters.
3. IRE with a steep pressure profile is identified as the pressure driven ballooning mode.
4. In TST-2, precursors of IRE with $n = 1$ and $n = 2$ are localized in the core ($\rho \sim 0.3$) and deform the plasma locally. This is very similar to IRE in MAST. A steep SXR profile is needed to trigger an IRE.
5. The ion temperature increase starts just after the occurrence of reconnection ($\sim 20 \mu\text{s}$).
6. Enhancement of localized deformation due to phase alignment between low- n modes is consistent with the result of simulation performed by Hayashi and Mizuguchi et al. The predicted pressure driven ballooning modes are confirmed in some cases.
7. MHD instabilities are classified. In contrast to ELMs at the edge of the plasma ($\rho > 0.8$) and sawteeth at $q \sim 1$, IREs occur in the intermediate region near the $q \sim 2$ surface and show different mode behaviour.
8. Techniques for poloidal mode analysis which is useful for MHD instability analysis has been improved. The three dimensional helical filamentary model is very effective for identifying the poloidal mode number in ST. This thesis confirmed three dimensional effects and the fitting

error is reduced by a factor of two compared with the axisymmetric model.

Acknowledgement

It is my great pleasure to complete this doctoral thesis. Firstly, I would like to thank the TST-2 team at the University of Tokyo. I would like to express my gratitude to my supervisor, Professor Yuichi Takase. He gave me a lot of valuable advises of general perspectives and chances of my visiting UKAEA. And, he was always cheering me. Associate professor Akira Ejiri gave me a lot of effective and detailed advises and skills for fundamental data analysis. Especially his contributions to the soft X-ray detectors I used for this thesis were essential. Dr. Yoshihiko Nagashima taught me how to install the electronic circuits and fluctuation analysis. Dr. Osamu Watanabe took me to places of recreation and relaxation at the laboratory excursions. Also, his good ideas contributed to the good quality of the draft of SXR detectors and its filters. I had fruitful discussions about the analysis with Mr. Yuuki Adachi. Also, other members, Mr. Takuya Oosako, Mr. Makoto Sasaki, Mr. Tetsuya Masuda, Mr. Takashi Yamaguchi, Mr. Byung Il An, Mr. Hiroki Kurashina, Mr. Hiroaki Kobayashi, Mr. Hiroyuki Hayashi, Ms. Haduki Matsuzawa Mr. Kotaro Yamada helped me through discussions and encouraged me.

Secondly, I am deeply grateful to the member of MAST team, UKAEA. The MAST team gave me a great experience as a researcher. Dr. Mikhail Gryaznevich, supervisor at Culham, always help me and give me good advises for not only experiments but also how to analyze the data in MAST. When I first went to Culham Science Centre, he welcomed me without any hesitations. He always supports me and help me to make the materials for international workshops, many times. Dr. Brian Lloyd gave me chances of IRE experiments in MAST and good advises for my abstracts for the workshops. Dr. Alan Sykes checked my materials and proceedings for the workshops. Mr. Dave Taylor taught me how to use EFIT and kEFIT in detail. Also, he explained me advises about the data server. Mr. John Storrs helped me for changing the digitizer settings at my machine time. He also encourages me and improved my English pronunciation. Dr. Garzotti Luca, working on the soft X-ray detectors, gave me the information (sight lines, coordinates,

frequency response etc.). Dr. Richard Martin, working on magnetic measurements, contribute to this thesis so much. Without his efforts, I could not do the analysis of the three dimensional filamentary models. Also, I would like to thank my friends in Culham who welcomed me. I enjoyed the life in England for about four months with them.

Finally my deep appreciation goes to my family and relatives. They have helped me so far. Without their help, I could not have the chance to complete this thesis.

This work was supported by JSPF Grant-in-Aid for Scientific Research 16106013, NIFS/NINS under the project of Formation of International Network for Scientific Collaborations and Global COE Program "the Physical Sciences Frontier", MEXT, Japan.

Bibliography

- [1] K.Miyamoto Fundamentals of Plasma Physics and Controlled Fusion Iwanamibook(1991).
- [2] John Wesson, Tokamaks, Clarendon Press-Oxford (1997).
- [3] R J Goldston and P H Rutherford Introduction to plasma physics Institute of Physics. Publishing Bristol and Philadelphia (2003)
- [4] F F. Chen Introduction to plasma physics Plenum Press New York (1974).
- [5] E. J. Strait, Physics of Plasmas **1**, 1415 (1994).
- [6] J. L. Johnson et al., Journal of Computational Physics **32** 212 (1979).
- [7] V. S. Mukhovatov and V. D. Shafranov, Nuclear Fusion **11** 605 (1971).
- [8] Y. -K. M. Peng and D. J. Strickler, Nuclear Fusion **26**, 769 (1986).
- [9] Y. -K. M. Peng, Nuclear Fusion **7**, 1692 (2000).
- [10] H. P. Furth and J. Killeen, Physics of Fluids **6**, 459 (1963).
- [11] Z. Chang et al., Physical Review Letters **74**, 46631 (1995).
- [12] R. J. La Haye et al., Nuclear Fusion **38**, 987 (1998).
- [13] A. Isayama et al., Proceedings of the 18th IAEA Fusion Energy Conference, Sorrento, IAEA-CN-77/EXP3/03 (2000).
- [14] D. A. Gates et al., Nuclear Fusion **37**, 1593 (1997).
- [15] H. Zohm et al., Nuclear Fusion **39**, 577 (1999).
- [16] G. Gantenbein et al., Physical Review Letters **85**, 1242 (2000).
- [17] M. Maraschek et al., Physical Review Letters **98**, 025005 (2007).

- [18] R. Prater et al., Proceedings of the 18th IAEA Fusion Energy Conference, Sorrento, IAEA-CN-77/EX8/1 (2000).
- [19] Y. Ikeda et al., Proceedings of the 18th IAEA Fusion Energy Conference, Sorrento, IAEA-CN-77/EXP4/03 (2000).
- [20] M. Maraschek et al., Physical Review Letters **45**, 1608 (2005)
- [21] A. Y. Aydemir et al., Physics of Fluids B **1** (1989).
- [22] S. von Goeler et al., Physical Review Letters **33**, 1201 (1974).
- [23] B.B. Kadomtsev, Soviet Journal of Plasma Physics **1**, 389 (1975)
- [24] A. Sykes and J.A. Wesson, Physical Review Letters **37**, 140, (1976).
- [25] J. A. Wesson, Plasma Physics and Controlled Fusion **28**, 243 (1986).
- [26] A. E. Edwards et al., Physical Review Letters **57**, 210 (1986).
- [27] R. S. Granetz and P. Smeulders, Nuclear Fusion **28**, 457 (1988).
- [28] H. K. Park et al., Physical Review Letters, **96**, 195004 (2006).
- [29] H. K. Park et al., Physical Review Letters, **96**, 195003 (2006).
- [30] H. K. Park et al., Plasma and Fusion Research, **2**, S1002 (2007).
- [31] I. H. Hutchinson, "Principle of Plasma Diagnostics " second edition, Cambridge University Press (2002).
- [32] W. Park et al., Physical Review Letters, **75**, 1763 (1995).
- [33] P. N. Yushmanov et al., Nuclear Fusion **30**, 1999 (1990).
- [34] F. Wagner et al., Physical Review Letters **49**, 1408 (1982).
- [35] F. Wagner et al., Proceedings of the 13th International Conference, Washington (1990), **1**, 277 (1991).
- [36] ITER Expert Group on Confinement and ITER Physics Basis Editor, Nuclear fusion **39**, 2175 (1999).
- [37] S. Von. Goeler et al., Nuclear Fusion **15**, 301 (1975).
- [38] A. Sykes et al., Nuclear Fusion **32**, 694 (1992).
- [39] A. Sykes, Physics of Plasmas **4**, 1665 (1997).

- [40] A. Sykes et al., Plasma Physics and Controlled Fusion **39**, B247 (1997).
- [41] T. C. Hender et al., Physics of Plasmas, **39**, 1958 (1999).
- [42] M. Ono et al., Nuclear Fusion **40**, 557 (2000).
- [43] I. Semenov et al., Physics of Plasmas **10**, 664 (2003).
- [44] ITER Physics Basis, Nuclear Fusion **39**, 2251 (2003).
- [45] D. Stutman et al., Review of Scientific Instruments **70**, 572 (1999).
- [46] E. J. Strait, Physics of Plasmas **1**, 1415 (1994).
- [47] T.R. Jarboe, Physics of Plasmas **5**, 1807 (1998).
- [48] J. Redd et al., Physics of Plasmas **9**, 2006 (2002).
- [49] University of Washington Plasma Science web page
([http : //www.aa.washington.edu/AERP/HIT/hit2_specification.html](http://www.aa.washington.edu/AERP/HIT/hit2_specification.html))
- [50] R. G. O'Neill et al., Physics of Plasmas **12**, 122506 (2005).
- [51] H. Tojo, Master thesis, The University of Tokyo (2005).
- [52] A. Ejiri et al., Nuclear Fusion **43**, 547 (2003).
- [53] N. Mizuguchi et al., Physics of Plasmas **7**, 3(2000).
- [54] N. Mizuguchi and T. Hayashi Journal of Plasma and Fusion Research **80**, 924 (2004).
- [55] T. Hayashi et al., Nuclear Fusion **40**, 721 (2000).
- [56] R. J. Hawryluk et al., Plasma Physics and Controlled Fusion **33**, 1509 (1991)].
- [57] Y. Nagayama et al., Physics of Fluids B **5**, 2571 (1993).
- [58] S. Mirnov et al., Physics of Plasmas **5**, 3950 (1998).
- [59] Y. Nagayama et al., Physics of Plasmas **61**, 3 (1990).
- [60] Y. Takase et al., Nuclear Fusion **41**, 11 (2001).
- [61] T. Oosako, Master thesis, The University of Tokyo (2005).
- [62] H. Kasahara, Doctoral thesis, The University of Tokyo (2005).

- [63] S. Kainaga et al., Plasma and Fusion Research, **3**, 027 (2008).
- [64] Y. Adachi et al., Review of Scientific Instruments, **79**, 10F507 (2008).
- [65] Y. Torii et al., Plasma and Fusion Research, **2**, 023 (2007).
- [66] J. Sugiyama et al., Plasma and Fusion Research, **3**, 026 (2008).
- [67] O. Watanabe et al., Plasma and Fusion Research, **3**, 049 (2008).
- [68] O. Watanabe et al., Proceedings at International Congress on Plasma Physics in 2008 (2008).
- [69] D. Smita, Doctoral thesis , University of Tokyo (2000)
- [70] R. Korde et al., Metrologia **43**, S145 (2003)
- [71] D. S. Gray et al., Review of Scientific Instruments **75**, 376 (2003)
- [72] I. Fumo et al., Review of Scientific Instruments **70**, 4552 (2003)
- [73] C. Suzuki et al., Review of Scientific Instruments **75**, 4142 (2004)
- [74] IRD Inc. (<http://www.ird-inc.com/axuvope.html>)
- [75] National Institute of Standards and Technology, website (<http://physics.nist.gov/PhysRefData/XrayMassCoef/cover.html>)
- [76] M.Yamamoto and S.Murayama Spectroscopic measurements of plasma Gakkai Shuppan center(2002)
- [77] S.Von.Goeler et al., Nuclear Fusion **25**, 1515(1985).
- [78] N. Iwama, Journal of Plasma and Fusion Research,**43**, 1310 (1998).
- [79] S. Ishida et al., Review of Scientific Instruments **61**, 2834 (1990).
- [80] C. Nardone, Plasma Physics and Controlled Fusion,**34**, 1447 (1992).
- [81] S. Yoshimura et al., Nuclear Fusion **9**, 3378 (2002).
- [82] S. Yoshimura et al., Physics of Plasmas **7**, 276 (2000).
- [83] B. Lloyd et al., Plasma Physics and Controlled Fusion **46**, B477 (2004)
- [84] B. Lloyd et al., Nuclear Fusion **43**, 1665 (2004)
- [85] UKAEA, web site (<http://www.fusion.org.uk/mast/index.html>)

- [86] B. Lloyd et al., The 13th International Workshop on Spherical Torus 2007 10 - 12 Oct 2007, Fukuoka, Japan. (<http://www.triam.kyushuu.ac.jp/ISTW2007/agenda.html>)
- [87] M. Walsh et al., Review of Scientific Instruments **70**, 742 (1999).
- [88] M. Walsh et al., Review of Scientific Instruments **74**, 1663 (2003).
- [89] R. Scannell et al., Review of Scientific Instruments **77**, 10E510 (2006).
- [90] R. Martin et al., Proceedings of 34th EPS Conference on Plasma Phys. Warsaw, P1-119 (2007).
- [91] L. L. Lao et al., Nuclear Fusion **25**, 1611 (1985).
- [92] L.C. Appel et al., Nuclear Fusion **41**, 169 (2001).
- [93] F.M. Levinton et al., Physical Review Letters **63**, 2060 (1989).
- [94] R. Jayakumar et al Fusion Science and Technology **48** 852 (2005).
- [95] R.J. Jayakumar et al., Nuclear Fusion **48**, 015004 (2008).
- [96] E.L. Foley et al., Nuclear Fusion **48**, 085004 (2008).
- [97] M.Kikuchi Nuclear Fusion, **26**, 101 (1986).
- [98] H.Tojo et al., Plasma and Fusion Research, **3**, S1065 (2008).
- [99] I. T. Chapman et al., Nuclear Fusion, **46**, 1009 (2006).